ACS OMEGA

Open Access

http://pubs.acs.org/journal/acsodf

Article

Design and Development of Sulfonamide-Chalcones as Antiepileptic Candidates: Computational and Zebrafish-Based Validation Approaches

Anis Nasuha Adzahar, Nik Nur Farhana Nik Aizan, Muhammad Alif Mohammad Latif, Muhammad Syafiq Akmal Mohd Fahmi, Ahmad Zaidi Ismail, and Siti Munirah Mohd Faudzi*

Cite This: *ACS Omega* 2025, 10, 55325−55353

Read Online

ACCESS | Metrics & More | Article Recommendations | Supporting Information

ABSTRACT: The study aims to develop safer and more effective antiepileptic drugs (AEDs) by targeting the γ-aminobutyric acid type A ($GABA_A$) receptor, an important inhibitory neurotransmitter system involved in the control of neuronal excitability and seizures. With epilepsy rates rising worldwide and current AEDs often causing serious side effects, new neurotherapeutics with better efficacy and safety are urgently needed. In this context, sulfonamides, known for their proven anticonvulsant properties, were selected as the core scaffold for the development of new sulfonamide−chalcone hybrids (compounds **1**−**36**) as potential AED candidates. These compounds were analyzed for their drug-likeness, ADMET profiles, and electronic properties using density functional theory (DFT) calculations. Molecular docking studies were then performed to examine their binding affinity to the $GABA_A$ receptor, revealing that the 4-(trifluoromethyl)sulfonamide-chalcones (**19**, **20**, and **21**) had the highest binding affinity (−10.3 to −10.1 kcal/mol) compared to the standard AED, valproic acid (VPA; −5.4 kcal/mol). To further support these findings, molecular dynamics (MD) simulations were performed with the top candidates. Analyses of root-mean-square deviation (RMSD), hydrogen bonding (H-bonds), radius of gyration (R_g), and solvent-accessible surface area (SASA) indicated that compound **20** exhibited the greatest stability throughout the simulation. Subsequently, to address toxicity risks, in vivo zebrafish mortality assays were performed to determine the LC_{50} values before proceeding to behavioral testing. All compounds showed a favorable safety profile and antiepileptic potential, as validated using a pentylenetetrazole (PTZ)-induced seizure zebrafish model. In conclusion, this integrated computational−experimental approach highlights the therapeutic potential of sulfonamide−chalcone hybrids, particularly 4-(trifluoromethyl)-*N*-(4-(3-(4-(trifluoromethyl)phenyl)acryloyl)phenyl)benzenesulfonamide (compound **20**), as potential positive allosteric modulators of the $GABA_A$ receptor, offering a viable pathway for the development of next-generation AEDs with improved efficacy and safety profiles.

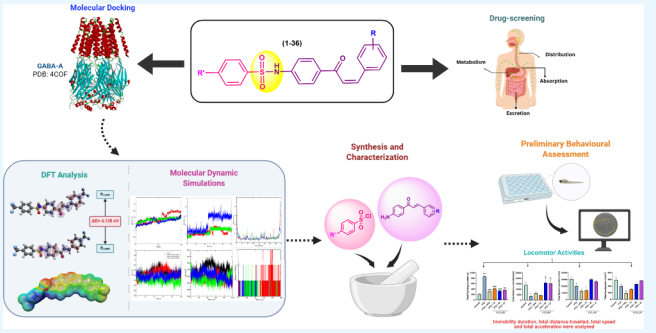

1. INTRODUCTION

Noncommunicable diseases (NCDs) contribute the most to global morbidity and mortality. Although neurological-associated NCDs account for 13% of the global burden of disease, they are often given too little priority, forming a "silent pandemic".[1] Epilepsy, also known as a seizure disorder, is a noninfectious neurological condition caused by abnormal brain cells that generate excessive hypersynchronous electrical signals, leading to rapid changes in behavior, cognitive function, and neurological deficits in individuals with epilepsy.[2,3] According to the Epilepsy Foundation, epilepsy has become a major global health concern, affecting nearly 71 million individuals of different ages, genders, races, and ethnicities. Alarmingly, 80% of epilepsy cases occur in low- and middle-income regions, including Malaysia.[4] Furthermore, according to the World Health Organization (WHO), epilepsy is the fifth leading cause of neurological disability-adjusted life years (DALYs), contributes to a growing number of premature deaths, and accounts for about 1% of the global burden of disease.[1] The increasing prevalence of epilepsy underscores the urgency of increased research into drug discovery and development to meet the diverse needs of those affected. Several options are available for the treatment of seizures, including antiepileptic drugs (AEDs), surgical interventions, and a ketogenic diet (KD). While these treatments can help

Received: May 22, 2025
Revised: October 19, 2025
Accepted: October 22, 2025
Published: November 13, 2025

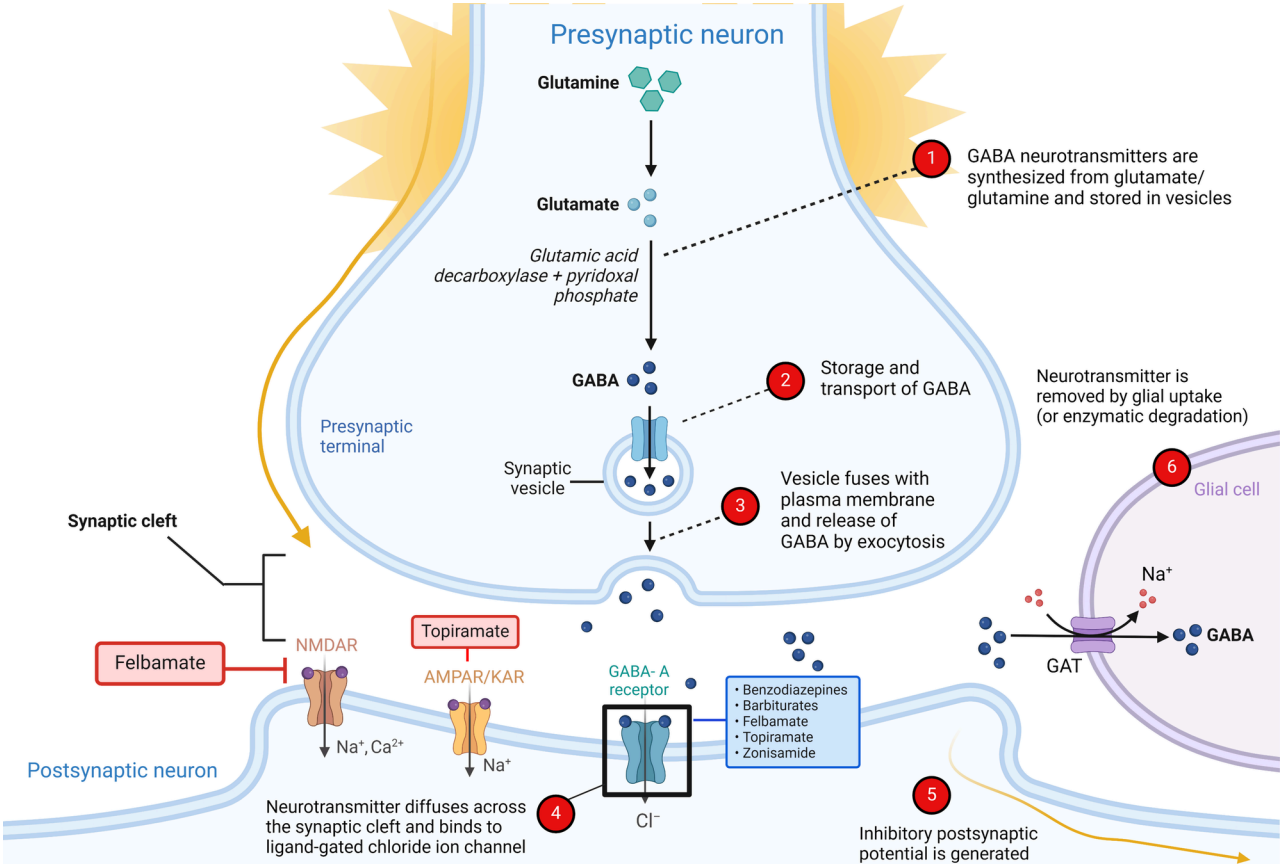

Figure 1. An overview of the γ-aminobutyric acid (GABA) signaling system.

control and manage seizures, no pharmacotherapy currently offers a complete cure for epilepsy.

AEDs are the common pharmacological treatment for epilepsy patients due to their proven efficacy in controlling seizures. Lifelong AED treatment, either in the form of monotherapy or polytherapy (a combination of two or more appropriate AEDs), has been shown to result in seizure freedom in approximately 70% of patients, depending on the type of seizure.[5] AEDs are divided into three classes: first, second and third generation AEDs, with valproic acid (VPA) being considered a representative of the first generation and remains a central role in epilepsy treatment. VPA is widely prescribed due to its broad efficacy against almost all forms of seizures. However, despite the availability of established AEDs, uncontrolled epileptic discharges still occur in about 25% of patients with drug-resistant epilepsy.[6] In addition, these drugs often pose a therapeutic challenge due to their adverse side effects, such as the significant risk of congenital malformations associated with valproate and its impact on the neurodevelopment of children born to women with epilepsy.[7] Prolonged administration of phenobarbital, zonisamide, and benzodiazepines (BZDs) can lead to nephrotoxicity, resulting in kidney disease and renal failure. In response to this unmet medical need, scientists are striving to design and develop new alternative AEDs that are both safer and more effective in controlling seizures, primarily to improve patients' quality of life while minimizing adverse effects.

While numerous potential factors may contribute to epilepsy, the exact mechanism of epileptogenesis remains elusive. Several neurotransmitters, including serotonin, dopamine, γ-aminobutyric acid (GABA), glutamate and noradrenaline, have been reported to play an important role in the mechanism of epilepsy and prevent the development of chronic epilepsy. There is growing evidence for the central role of GABA in both the development and prevention of seizures. GABA, a key inhibitory neurotransmitter in the mammalian brain, binds to the orthosteric GABA binding site and activates two types of receptors upon release into the synaptic cleft: ionotropic $GABA_A$ receptors and metabotropic $GABA_B$ receptors.[8] An overview of the GABA signaling system is shown in Figure 1. It has been concluded that the absence of GABAergic processes may increase a person's susceptibility to epilepsy. Therefore, the development of new AEDs is focused on improving the mechanism of action that enhances GABA-mediated neuronal inhibition.

Chalcones, are "open-chain" precursors in the biosynthesis of flavonoids and isoflavonoids in edible plants. Natural and synthetic chalcones exhibit various pharmacological activities, including anticancer, antimicrobial, anti-inflammatory, and anticonvulsant effects.[9] Chalcone and its derivatives have been investigated as potential positive allosteric modulators of GABA, as they are sufficiently lipophilic to penetrate the blood−brain barrier (BBB).[10,11] In addition, their low total polar surface area (TPSA) is important for the development of new therapeutics for neurological disorders, including epilepsy, allowing them to penetrate the BBB and act in the CNS.[12] On the other hand, sulfonamides have been used as a primary treatment for many infectious diseases since 1941, before the introduction of penicillin.[13] In antiepileptic therapy, sulfonamides are known to improve GABAergic neurotransmission. Zonisamide[14] and sulthiame[15] (Figure 2), for example, have an anticonvulsant effect and achieve good CNS penetration, partly

https://doi.org/10.1021/acsomega.5c04809
ACS Omega 2025, 10, 55325−55353

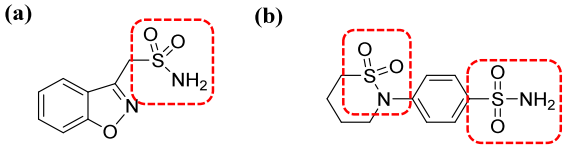

Figure 2. Sulfonamide derivatives used as AEDs; (a) zonisamide and (b) sulthiame. Sulfonamide moiety is highlighted within the red box.

by inhibiting carbonic anhydrase (CA). While these agents are generally effective in controlling seizures, they are associated with psychiatric and cognitive side effects in some patients, occasionally leading to treatment discontinuation.

In our previous studies, we identified several chalcone-based compounds (Figure 3a), including pyrrolylated and trimethoxylated chalcones, that have significant antiepileptic and anxiolytic activity in both chemically induced [acute pentylenetetrazole (PTZ)] and genetic zebrafish epilepsy models (e.g., *gabra1*, gabrg2, *zc4h2* knockouts).[16] Of note, the seizure suppressive effect of trimethoxylated chalcones was abolished by flumazenil, a $GABA_A$ receptor antagonist, suggesting GABAergic modulation as the primary mechanism.[17] These findings established the chalcone scaffold a promising platform for the development of GABA-targeted AEDs. Building on this, structure activity relationship (SAR) studies have consistently shown that the incorporation of *para*-electron withdrawing groups, such as $-CF_3$, significantly enhances neuroactivity by improving metabolic stability, lipophilicity, blood−brain barrier (BBB) permeability, and receptor binding affinity. This effect is well illustrated by clinically used CNS drugs such as fluoxetine and fluphenazine.[18] Based on this SAR rationale, we strategically introduced the $-CF_3$ group at the key positions of the sulfonamide and chalcone rings. In parallel, we replaced the pyrrole moiety with a phenylsulfonamide group (Figure 3b) to improve hydrogen bonding and electrostatic complementarity with the $GABA_A$ receptor. This dual modification strategy was expected to improve binding affinity, pharmacokinetic properties and overall drug likeness. To rationalize and evaluate this design, we applied in silico methods, including absorption, distribution, metabolism, excretion and toxicity (ADMET) predictions, molecular docking and molecular dynamics (MD) simulations to systematically evaluate binding and therapeutic potential.

This approach is in line with recent advances in computational drug discovery, where techniques such as virtual screening, pharmacophore modeling, and quantitative structure−activity relationships (QSAR) analysis have become essential for rapid prediction of biological activity and lead optimization. By efficiently screening large chemical libraries, these methods help identify AED candidates with optimal potency, selectivity, and safety, significantly reducing the reliance on time-consuming in vivo experiments. For example, the discovery and optimization of perampanel, a selective AMPA receptor antagonist approved for epilepsy treatment, leveraged structure-based virtual screening and molecular docking to improve its binding affinity and selectivity.[19,20] Similarly, computational approaches guided the design of lacosamide, which targets voltage-gated sodium channels and has improved pharmacokinetics and a better safety profile.[21] More recently, artificial intelligence (AI) approaches, including machine learning (ML) and deep learning (DL), have expended computational drug discovery capabilities. These tools have further improved predictive accuracy in ADMET properties, pharmacokinetics, toxicity, and polypharmacological modeling, which are critical for epilepsy treatments, that often require polytherapy. For instance, deep neural networks (DNNs) and graph neural networks (GNNs) have demonstrated high predictive accuracy for CNS parameters, including BBB permeability and neurotoxicity risk, both of which are critical considerations in antiepileptic drug development.[22,23] With this data-driven approach, issues such as BBB penetration and metabolic stability can be identified early, increasing the likelihood of clinical success. Ultimately, these computational innovations streamline the discovery of AEDs and enable the development of safer and more effective therapies tailored to the complex needs of epilepsy patient.[24]

Due to their genetic similarity to humans, zebrafish (*Danio rerio*) have become a prominent vertebrate model in drug discovery research, particularly for neurological diseases. Approximately 82% of human disease-associated genes have identifiable orthologues in zebrafish. In addition to their physiological and developmental similarities to humans, zebrafish offer several key advantages over rodents that have been conventionally used in epilepsy research. These advantages include rapid development and their transparent appearance that allow real-time visualization of neurological activity.[25] Their small size and ease of maintenance also enable high-throughput experiments, making them ideal for large-scale genetic and pharmacological studies.[26] Besides that, their blood−brain barrier (BBB), a critical regulatory interface between the circulatory system and the central nervous system (CNS), has structural and functional parallels to the mammalian BBB.[27] These features make zebrafish an invaluable tool for studying drug delivery and neuroprotective

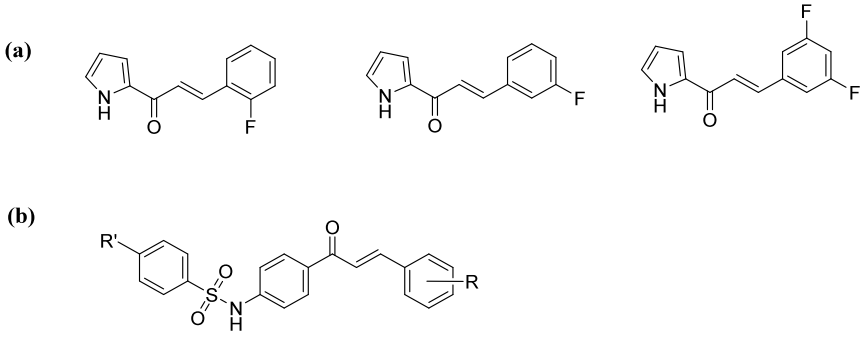

Figure 3. Structures of (a) the pyrrolylated-chalcones active in both chemically induced and genetic epilepsy zebrafish in vivo models and (b) the newly designed sulfonamide-containing chalcones.

https://doi.org/10.1021/acsomega.5c04809
ACS Omega 2025, 10, 55325−55353

Table 1. Newly Designed Intermediate 4-Aminochalcones (Series I; 1−12), the Targeted 4-(Trifluoromethyl) Benzenesulfonamide-Containing Chalcones (Series II; 13−24), and the Targeted 4-(Methoxyl)benzenesulfonamide-Containing Chalcones (Series III; 25−36)

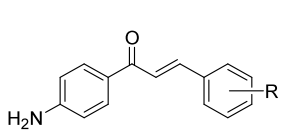

Series I

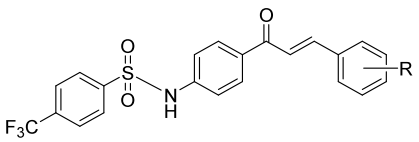

Series II

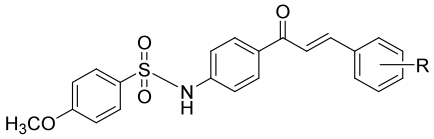

Series III

R	series I (compound)	series II (compound)	series III (compound)
H	**1**	**13**	**25**
2-methoxyl	**2**	**14**	**26**
4-methoxyl	**3**	**15**	**27**
2-fluoro	**4**	**16**	**28**
3-fluoro	**5**	**17**	**29**
4-fluoro	**6**	**18**	**30**
3-(trifluoromethyl)	**7**	**19**	**31**
4-(trifluoromethyl)	**8**	**20**	**32**
4-bromo	**9**	**21**	**33**
4-chloro	**10**	**22**	**34**
3,4-difluoro	**11**	**23**	**35**
3,5-difluoro	**12**	**24**	**36**

Table 2. Comprehensive Summary of ADMET Parameters with Algorithmic Bases and Performance Metrics for ADMETlab 3.0[b]

ADMET end points	model/algorithm	uncertainty method[a]	performance metric	confidence threshold	error margin/ threshold
human intestinal absorption (HIA)	multitask DMPNN with bond-level message passing + RDKit 2D descriptors	evidential deep learning	[a]AUC = 0.89 ± 0.03	high confidence if >0.7	Youden's index cutoff
blood−brain barrier (BBB)	graph attention-enhanced DMPNN	Monte Carlo dropout	AUC = 0.90	high confidence if variance, σ^2 < 0.15	±0.15 variance
plasma protein binding (PPB)	multitask DMPNN regression with RDkit descriptors	evidential epistemic/ aleatoric	R^2 = 0.85	based on RMSE uncertainty range	±0.3 log units
CYP2C19 inhibition	hybrid DMPNN + XGBoost	Monte Carlo dropout	AUC = 0.89	binary high/Low classification	statistical intervals
P-glycoprotein (PgP) inhibition	DMPNN with adversarial training	Monte Carlo dropout variance	AUC = 0.85−0.92	binary high/Low classification	dropout variance range
genotoxicity	multitask DMPNN classification	evidential deep learning	AUC = 0.73−0.96	maximum Youden's index	confidence scores threshold
drug-induced neurotoxicity	DMNN with graph convolution	Monte Carlo dropout	AUC = 0.80−0.89	variance-based threshold	variance limit
respiratory toxicity	multitask DMPNN framework	Evidential uncertainty	AUC = 0.76−0.88	binary confidence	distribution parameters
skin sensitization	DMPNN + RDKit descriptors	Monte Carlo dropout	AUC = 0.82−0.91	confidence threshold	ensemble variance
AMES mutagenicity	graph neural network DMPNN	evidential deep learning	AUC = 0.85−0.93	probability entropy threshold	epistemic uncertainty
carcinogenicity	multitask DMPNN	Monte Carlo dropout	AUC = 0.78−0.87	calibrated confidence intervals	uncertainty scores

[a]AUC (Area under curve); DMPNN = directed message passing neural network. [b]Reproduced and summarized from Fu et al.,[32] with permission from Oxford University Press.

mechanisms in the CNS.[27] Zebrafish larvae also show seizure-like behaviors, such as rhythmic body convulsions and irregular swimming patterns, which closely resemble to human epileptic symptoms.[25,28] These behaviors are easily observable and can be quantitatively analyzed by automated tracking systems to evaluate the efficacy of AEDs. Overall, zebrafish have become an indispensable tool in epilepsy research, that offering rapid development and genetic homology that facilitate comprehensive neurological studies. Therefore, they are included in the present study for the experimental validation of the computational predictions.

2. MATERIALS AND METHODS

2.1. Drug-Likeness Predictions. *2.1.1. Data Set Selection.* In this study, two in silico techniques, molecular docking and MD simulations, were used to predict the potential antiepileptic activity of three series of newly designed compounds (**1−36**), focusing on the inhibition of the GABA neurotransmitter. These series include the intermediate compound, 4-aminochalcones (Series I), as well as the 4-(trifluoromethyl)benzenesulfonamide-containing chalcones (Series II) and the 4-(methoxyl)benzenesulfonamide-contain-

https://doi.org/10.1021/acsomega.5c04809
ACS Omega 2025, 10, 55325−55353

ing chalcones (Series III), with structures of which are outlined in Table 1.

2.1.2. Prediction of Physicochemical, Pan-Assay Interference Compounds (PAINS), and Aggregation Properties for Drug-Likeness Assessment. The concept of drug-likeness evaluates the likelihood that a molecule is suitable for the formulation of an oral treatment primarily based on its bioavailability, which is assessed by its structural and physicochemical properties. To ensure compliance with drug-like characteristics, the newly designed sulfonamide-chalcones (compounds **1**−**36**) must fulfill the established criteria of Lipinski's Rule of Five (RO5), EGAN and VEBER rule, as listed in Table 2. In this study, the intended physicochemical characteristics were predicted using the open online server FAF-Drugs4 v4.0 (https://mobyle2.rpbs.univ-paris-diderot.fr/cgi-bin/portal.py#forms::FAF-Drugs4). First, Chemdraw Ultra 12.0 software was used to generate the Simplified Molecular Input Line Entry System (SMILES) for all designed compounds. Subsequently, the SMILES were submitted to the FAF-Drugs4 Bank Formatter (https://mobyle2.rpbs.univ-paris-diderot.fr/cgi-bin/portal.py#forms::Bank-Formatter) to be converted into the Symyx Spatial Data File (SDF) format compatible with the server. The produced SDF files were later transferred to the FAF-Drugs4 Web Server as an input file. Furthermore, the SwissADME v2017 tool (http://www.swissadme.ch/), was used to predict water solubility (log*S*) and potential pan-assay interference compounds (PAINS). This platform uses Support Vector Machines (SVM) with Radial Basis Function (RBF) Gaussian kernels, implemented with libSVM v3.20, trained on molecular and physicochemical descriptors with 10-fold cross-validation for model optimization. This machine-learning (ML) approach has outperformed other algorithms in binary classification tasks and is therefore suitable for the prediction of pharmacokinetic properties. By integrating empirical rules and ML models, the platform is able to predict key pharmacokinetic end points such as solubility, lipophilicity and bioavailability.[29] As part of the evaluation process, the SMILES strings of all compounds generated in the previous step were loaded into the SwissADME web tool. Among the available models, the Estimated Solubility (ESOL) model developed by Delaney was selected due to its robust performance in predicting aqueous solubility (log*S*) based on molecular weight, calculated log*P*, proportion of heavy atoms in the aromatic rings and number of rotatable bonds, and achieves good accuracy in estimating solubility within a factor of 5 to 8. SwissADME v2017 issues warnings when such substructural alert are detected in the tested molecules, and will displays a 0 notice when a non-PAINS structure is identified.[30] Subsequently, the SDF file was uploaded to the ChemAGG web platform (https://admet.scbdd.com/ChemAGG/index/) to predict the likely aggregators in the newly designed chalcones. The aggregator prediction results were categorized into two different categories: Aggregator (1) and nonaggregator (0). In addition, fraction of sp^3 carbon atoms (Fsp^3) and phospholipidosis (PLD) analysis was performed to measure the additional drug-likeness properties using ADMETlab prediction tools (https://admet.scbdd.com/calcpre/index/#).

2.1.3. Absorption, Distribution, Metabolism, Excretion, and Toxicity (ADMET) Analyses. In drug discovery and development, it is critical to consider pharmacokinetic factors such as absorption, distribution, metabolism, excretion, and toxicity (ADMET) when assessing the potential efficacy and bioavailability of a drug candidate. In this study, ADMETlab 3.0 (2024 release) was used to predict the ADMET properties of the newly designed compounds (**1**−**36**) and to compare them with the AEDs on the market. ADMETlab 3.0 integrates a "Directed Message Passing Neural Network" (DMPNN) framework which leverages RDKit v2023.3.3 for 2D molecular descriptor calculation in Chemprop v1.6.1.[31] An important advance in ADMETlab 3.0 is the implementation of evidential deep learning to quantify prediction uncertainty, which provides confidence scores (from 0 to 1) and associated margins of error for each prediction.[32] This enables a robust assessment of prediction reliability and model performance. All ADMET parameters analyzed in this study are tabulated in Table 2 along with the corresponding algorithmic bases, uncertainty methods, performance metrics and confidence thresholds. First, the existing SMILES (created to predict the physicochemical properties) were imported as an entry into the ADMETlab 3.0 server to generate the ADME profiles. Compounds were scored based on their predicted absorption for BBB, human intestinal absorption (HIA), plasma protein binding (PPB), and CYP2C19 gene, considering the characteristics that define their drug-like pharmacokinetic profile. Additionally, an in silico toxicity screening was performed using the free ADMETlab 3.0 Web. A single SMILES string of each compound was inserted and submitted to the web server. The result can be downloaded as a.pdf file containing all predicted toxicity values for genotoxicity, drug-induced neurotoxicity, respiratory toxicity, skin sensitization, rat toxicity, AMES mutagenicity, and carcinogenicity. It is important to note that all ADMET parameter predictions achieved consistently high discriminatory power (AUC $\geq$ 0.78) with robust performance across different end points and algorithms, confirming the reliability and predictive accuracy of the integrated assessment platform, as summarized in Table 2.

2.2. Molecular Docking. Molecular docking, a widely used computational technique in structure-based drug design (SBDD), plays a significant role in modern drug discovery. This method enables the visual evaluation of potential drug candidates (**1**−**36**) at the allosteric site of the $GABA_A$ receptor by accurately analyzing the potential interactions, binding modes, and binding affinity.

2.2.1. Protein Preparation. The cocrystallized structure of the $GABA_A$ receptor ($GABA_AR$, PDB ID: 4COF) served as the target protein for docking, as it has the highest expression level in the CNS and is mainly responsible for rapid inhibition in the brain among the GABA receptors.[33] The $GABA_AR$ is the most abundant and important receptor of the GABA system involved in the modulation of seizure activity.[34,35] The crystal structure of the target protein, $GABA_A$ receptor beta3 homopentamer (PDB ID: 4COF),[36] was retrieved in.pdb format from the RCSB Protein Data Bank (PDB; https://www.rcsb.org/). The X-ray diffraction structure of the $GABA_AR$ had a resolution of 2.97 Å, an *R* value of 0.206, and a free *R* value of 0.226. The unit cell parameters were described as follows: Length [Å] a = 174.10, b = 108.90, c = 207.44, Angle [°] α = 90.00, β = 107.43, γ = 90.00. Before subjecting the target protein to molecular docking, it must be preprocessed. The protein was first prepared by removing water molecules, cocrystallized ligands and heteroatoms using Discovery Studio Visualizer v19.1.0.18.287 (BIOVIA Dassault Systèmes, CA, USA). Polar hydrogens were then added and default Kollman charges were assigned to the macromolecule atoms using AutoDock Tools version 1.5.6. Upon completion

https://doi.org/10.1021/acsomega.5c04809
ACS Omega 2025, 10, 55325−55353

of receptor preparation, the prepared receptor was saved in.pdbqt format for docking studies.

2.2.2. Ligand Preparation. The 2D chemical structures of the newly designed sulfonamide chalcones (compounds **1**−**36**) and the standard drug VPA were drawn using ChemDraw Ultra 12.0 to generate the SMILES notation. This notation was then converted to 3D structures, optimized using the General Amber Force Field (GAFF) with the steep descent algorithm in 10 steps, and saved in.pdb format using Avogadro software. GAFF is a widely used force field for small molecules designed to accurately represent a broad spectrum of molecules and capture the majority of organic chemical space. The Gasteiger charges were then assigned to ligand atoms using AutoDock Tools version 1.5.6 and saved in.pdbqt format.

2.2.3. Protein−Ligand Docking. The $GABA_AR$ was selected as the primary target for molecular docking studies to evaluate its antiepileptic efficacy. All ligands, including the reference drug VPA, were docked to the allosteric site of the $GABA_AR$ using the cocrystallized ligand benzamidine as a reference. Molecular docking was performed using a 40 × 40 × 40 $Å^3$ grid box, the grid spacing was set to 1.0 Å, and the exhaustiveness parameter was set to 8. Docking was centered on the entire protein, with coordinates (−20.809, −17.349, 122.90) for the $GABA_AR$. The Broyden−Fletcher−Goldfarb−Shanno algorithm (BFGS run) served as the primary optimization algorithm for molecular docking. AutoDock Vina version 1.1.2 (https://vina.scripps.edu) from the Scripps Research Institute was used to generate a series of nine conformations arranged in descending order of docking score. The docking procedure began after the receptor's allosteric binding pocket was located, its dimensions and position determined, and the size of the docking zone established. After the docking simulation, the most favorable conformation of the ligand within the binding sites was analyzed using Discovery Studio Visualizer v19.1.0.18.287. Upon docking, the root-mean-square deviation (RMSD) is computed to determine the discrepancy between the predicted pose and the experimentally docked pose. The benzamidine conformations with the highest rank and the lowest RMSD value of 0.6835 were selected. Virtual screening of all newly designed chalcone derivatives (compounds **1**−**36**) and the known GABA antagonist VPA was performed with the same docking parameters.

2.2.4. Docking Protocol Validation and ROC-AUC Analysis. To evaluate the performance of the virtual screening and the discriminatory power of the molecular docking protocol, a receiver operating characteristic (ROC) curve analysis was conducted in accordance with established benchmarking guidelines. The validation data set comprised 3 known compounds and 84 property-matched decoys generated with DeepCoy,[37] maintaining a 1:28 active-to-decoy, which is in line with accepted virtual screening standards. ROC curves were generated by plotting the true positive rate (sensitivity) against the false positive rate (1 − specificity) over a range of docking score thresholds. The area under the ROC curve (AUC) was calculated as a quantitative measure of the protocol's ability to discriminate between active compounds and decoys, with AUC values approaching 1.0 indicating excellent predictive performance. This analysis also provides information on early detection, a crucial factor in the practice of virtual screening. To further assess statistical robustness, enrichment factors (EF) were calculated for the top 1 and 5% of the ranked database. Enrichment factors significantly greater than 1.0 indicate that the protocol is better than random selection. The EF values were calculated using the following formula:

$$EF_x\% = \frac{\text{Database\_screened}_x\%/\text{Total\_database}}{\text{Actives\_found}_x\%/\text{Total\_actives}}$$

In this study, the molecular docking scores of two well-characterized $GABA_A$ ligands were used as benchmark to define the threshold for high-binding affinity ligand. Benzamidine, a cocrystallized orthosteric ligand, docked at −6.7 kcal·mol^{-1}, while VPA, a clinically used anticonvulsant that modulates GABAergic activity, docked at −5.4 kcal·mol^{-1} according to our docking protocol. Accordingly, any ligand with a docking score ≤−6.7 kcal·mol^{-1} was classified as 'high-affinity,' as it met or exceeded the binding strength of a validated orthosteric reference. This threshold is consistent with literature reports on $GABA_A$ modulators such as BZDs (−7 to −8 kcal·mol^{-1}),[38] which emphasizes its physiological relevance.

2.3. Fragment-Based Molecular Docking and Substructure SAR. *2.3.1. Receptor Preparation.* The X-ray structure of human CYP2C19 (PDB ID: 4GQS, resolution: 2.10 Å) was retrieved from the RCSB Protein Data Bank (https://www.rcsb.org/). All crystallographic water molecules, buffer ions, and nonessential heteroatoms were removed using BIOVIA Discovery Studio v19.1. Polar hydrogens were added and Kollman charges assigned using AutoDockTools v1.5.6, after which the receptor was exported in.pdbqt format.

2.3.2. Ligand and Fragment Preparation. Seven representative substructures of sulfonamide-chalcones were selected to study the SARs: (i) sulfonamide (−SO_2NH−), (ii) trifluoromethyl (−CF_3), (iii) chalcone C3-linker (−CO−CH═CH−), (iv) phenyl (−C_6H_5), and monatomic halogens (v) fluorine (−F), (vi) chlorine (−Cl), and (vii) bromine (−Br). The 2D structures were drawn in ChemDraw 12, converted to 3D conformations via Avogadro 1.97 and energy-minimized using the MMFF94 force field. The Gasteiger partial charges were subsequently assigned with AutoDockTools and the resulting files were saved in .pdbqt format.

2.3.3. Docking Protocol. Rigid-receptor docking was performed with AutoDock Vina v1.2.7 under the same conditions as the previously described full-molecule screening (Section 2.2.3). The docking search space was defined to enclose the prosthetic heme group (HEM501) and the central iron atom (Fe), which is the primary catalytic site of CYP2C19. Accordingly, the grid box was centered at the coordinates (x = −79.463 Å, y = 15.477 Å, z = −44.783 Å) and dimensions 20 × 20 × 20 $Å^3$, ensuring whole coverage of the haem pocket and adjacent substrate recognition sites. An exhaustiveness of 16 and the default energy range of 3 kcal·mol^{-1} were used. Ten docking poses were generated for each fragment and ranked according to their predicted binding affinity (ΔG). The lowest-energy pose was selected for ligand efficiency (LE) calculations, as $LE = \frac{|\Delta G|}{N_{heavy}}$; where ΔG is the docking score (kcal/mol) and N_{heavy} is the number of non-hydrogen atoms. The key molecular interactions (H-bonds, halogen bonds, $\pi-\pi$ and hydrophobic contacts) were analyzed using Discovery Studio Visualizer, selecting residues within a 4 Å radius of each fragment.

2.4. Density Functional Theory (DFT) Calculation. Quantum chemical methods such as density functional theory (DFT) were calculated for the predicted active compounds using the ORCA (version 6.0.1),[39] Avogadro, and ChemCraft

https://doi.org/10.1021/acsomega.5c04809
ACS Omega 2025, 10, 55325−55353

version 1.8 (https://www.chemcraftprog.com) for molecular visualization. First, the selected structures (compounds **19**, **20**, and **21**) were prepared using the Avogadro software and then optimized at the B3LYP/6-31g(d,p) level of theory in the gas phase using Gaussian 09 suite program.[40] For compounds **19**, **20**, and **21**, the three-parameter hybrid functional of Becke in the ground state was used using the correlation of Lee, Yang, and Parr (B3LYP) with the def-SV(P) basis set. The distribution of electrons in the highest occupied molecular orbital (HOMO) and the lowest unoccupied molecular orbital (LUMO) is the most important reference when studying the reactivity of molecules. The input file was generated by inserting the ground-state calculation into the DFT framework. The parameters and visualization of the molecule from the DFT calculation were processed and displayed using the ChemCraft version 1.8 program (https://www.chemcraftprog.com). The output file contains the HOMO energy (E_{HOMO}) and the LUMO energy (E_{LUMO}). Subsequently, both the E_{HOMO} and E_{LUMO} were used to calculate the other global reactivity parameters such as the gap energies (ΔE_{gap}) (eq 1), the ionization potential (IP = $-E_{HOMO}$), the electron affinity (EA = $-E_{LUMO}$), the electronegativity (χ) (eq 2), the chemical potential (μ) (eq 3), the global hardness (η) (eq 4), the global softness (s) (eq 5) and the electrophilicity index (ω) (eq 6). DFT complements molecular docking by providing insights into the electronic properties, reactivity and stability of the compounds, thus contributing to a better understanding of their potential interactions with the target protein.

$$\Delta E_{gap} = E_{HOMO} - E_{LUMO} \quad (1)$$

$$\chi = (IP + EA)/2 \quad (2)$$

$$\mu = -(IP + EA)/2 \quad (3)$$

$$\eta = (IP - EA)/2 \quad (4)$$

$$s = 1/2\eta \quad (5)$$

$$\omega = \mu^2/2\eta \quad (6)$$

2.5. Molecular Dynamics (MD) Simulations. MD simulations are widely used computational methods in drug discovery that provide researchers with detailed insights into the dynamic behavior of biomolecules, such as proteins, and their interactions with ligands at the atomic level.[41] This approach enables rational experimental design and provides access to complex data and models. In particular, MD simulations predict how a molecule binds to a protein and the effects this has on protein structure, including fluctuations or conformational changes over time using Newton's laws.[42] In the postdocking assessment, only the top three chalcone-protein complexes, compounds **19**, **20**, and **21** (selected based on docking score and interactions), were subjected to MD simulation using the GROningen MAchine for Chemical Simulations (GROMACS) for each docking parameter. The MD process begins with the preparation of the protein and selected ligand structures from Section 2.2. First, the .pdbqt files of the docked protein−ligand complexes are displayed in PyMOL. The settings "retain_order" and "pdb_retain_ids" are switched off (set to 1) before they are exported to a single .pdb file. The coordinates, residue names, atom names and essential ligand information are then extracted from the original docked.pdb file and transferred to a new text file to separate the.pdb files of the protein and ligand structures. The MD simulations then start with two files: "ligand.pdb" and "protein.pdb". The polar hydrogen atoms are added to the ligand using Discovery Studio Visualizer v19.1.0.18.287 before being uploaded to the LigParGen web server (https://zarbi.chem.yale.edu/ligpargen/). LigParGen was used in this MD study to generate all-atom optimized potentials for liquid simulations (OPLS-AA) force field parameters for ligands using 1.14*CM1A(-LBCC) loaded models,[43] and to provide GROMACS-compatible input files for MD simulations. The .itp and .gro files of the ligands were acquired from the LigParGen web and used in GROMACS.

Once the parameter files for both the ligand and protein are created, the pdb 2gmx program was used to generate the topology file. This is an essential step in the preparation of MD simulations, which includes the selection of the appropriate force field. The topology file contains important details about the connectivity, geometry and parameters of the system that are required for the MD simulation of proteins, nucleic acids or other biomolecules. The required files, such as the.pdb file for the protein and the ligands as well as the ITP file for the ligands, are transferred with the Xftp program. The three-point water model, in particular the simple point charge (SPC) water model, is used in a cubic unit cell with the initial dimensions of 148.54 × 148.54 × 148.54 Å^3. The protein is positioned at a minimum distance of 1.0 nm from the edge of the box. In addition, 98,329 water molecules and 9 molecules of Cl^- are introduced into the targeted $GABA_AR$ to equilibrate the system. The complex reduces its energy through heating and equilibrium processes using the OPLS-AA force field before the MD simulations begin. The steepest descent method is used to minimize the complexes, followed by heating in the range of 0 to 300 K. The selected three ligand-protein structures are stabilized at 300 K for 100 ps under *NVT* boundary conditions (constant simulation cell volume (V) and temperature (T)). Subsequently, an MD simulation is performed under *NPT* boundary conditions for 100 ps at a constant temperature (T) and pressure (P) of 300 K and 1 atm, respectively, using an integration time step of 2 fs. The final production run takes 100 ns, with time steps of 100,000 ps, a temperature of 300 K and a pressure of 1.01325 atm. The Nose−Hoover method with *NPT* ensemble is used for both complexes. Long-range electrostatic interactions were calculated using the Particle Mesh Ewald (PME) method with a Coulomb cutoff value of 1.2 nm.[44] The Lincs method fixes all bond lengths involving hydrogen atoms during the simulations.[45] The stability of each ligand−protein complex was assessed using 100 ns MD trajectories analyzed with GROMACS 2021.1. Key structural metrics, including RMSD, root-mean-square fluctuations (RMSF), radius of gyration (Rg) and solvent-accessible surface area (SASA) were calculated to assess the stability of the complex. Intermolecular H-bonds were identified with gmx hbond using standard criteria (donor−acceptor distance $\leq$ 0.35 nm; hydrogen donor−acceptor angle $\geq$ 150°), and H-bond lifetimes (τ_{HB}) were derived from autocorrelation integrals. Two parameters, ligand RMSD and τ_{HB}, were selected to investigate correlations with docking affinities. The resulting time series were exported as XVG files, converted to CSV and processed in Python to calculate average values. These were plotted against the AutoDock Vina docking scores and statistical relationships were assessed using Pearson correlation coefficients (r), p-values and coefficients of determination (R^2). Structural visualizations were created using the Visual Molecular

https://doi.org/10.1021/acsomega.5c04809
ACS Omega 2025, 10, 55325−55353

Scheme 1. General Synthesis Route for Sulfonamide-Chalcones (Compounds 19, 20, and 21) via Two-Step Reactions

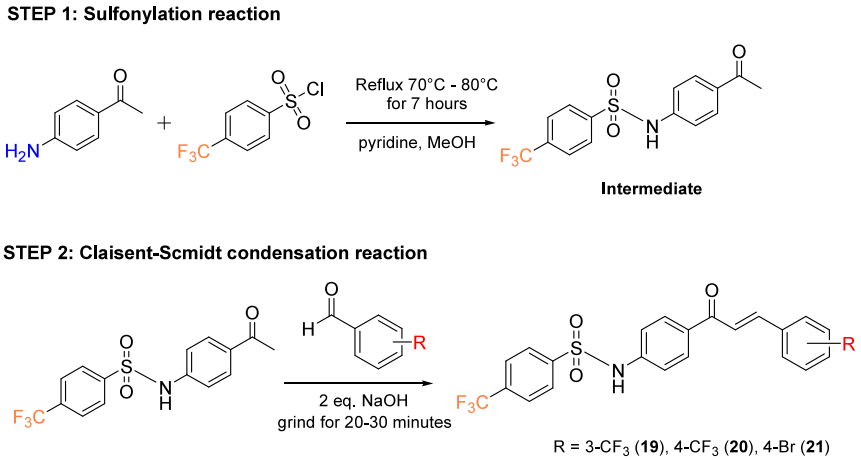

Dynamics (VMD), which also supported additional trajectory inspection and data extraction.

2.6. Synthesis of Sulfonamide Chalcones. *2.6.1. General.* All starting materials, reagents and solvents were purchased from Merck, Sigma-Aldrich, and Thermo Fischer Scientific, and used directly without further purification. The solvents used for the spectroscopic measurements were of spectroscopic grade. All synthesized compounds were monitored by thin layer chromatography (TLC) with precoated aluminum sheets on silica gel 60 F254 (layer thickness 0.2 mm, Merck), while column chromatography was performed with silica gel 60 (70−230 mesh ASTM, Merck). The FT-IR spectrum of the synthesized compound was recorded using an FT-IR spectrometer (PerkinElmer RX1, Massachusetts, USA) in the mid-IR region (400−4000 cm^{-1}) using the Attenuated Total Reflectance (ATR) technique. The direct injection mass spectra (DI-MS) were measured with a GCMS-QP2010 Plus (Shimadzu). ^{1}H and ^{13}C NMR spectra were recorded in methanol-d_4 (CD_3OD) using a Varian 500 MHz NMR spectrometer (Varian Inc., Palo Alto, CA). Melting points were determined using a Fisher-Johns melting point apparatus.

2.6.2. General Procedure for the Synthesis of N-(4-Acetylphenyl)-4-(trifluoromethyl)benzenesulfonamide Intermediate. Three selected sulfonamide chalcones with the highest docking scores (compounds **19**, **20**, and **21**) were chosen for synthesis, via two steps, sulfonylation and the Claisen-S cmidt condensation reaction (Scheme 1). First, pyridine (10 mL) was added to a solution of 4-aminoacetophenone (0.6887 g, 5 mmol) in methanol (25 mL) and the reaction mixture was stirred at room temperature for 10 min. Then, 4-trifluoromethylsulfonyl chloride (505.4 μL, 10 mmol) was added dropwise and the mixture was stirred at 70−80 °C for 5−7 h under reflux. Upon completion of the reaction (monitored by TLC), the reaction mixture was cooled to room temperature. To quench unreacted sulfonyl chloride and stop the reaction, ice-cold water was carefully added. The organic extracts were combined and dried over anhydrous magnesium sulfate ($MgSO_4$) to remove residual water. The desiccant was removed by gravity filtration and the organic solvents were removed under reduced pressure using a rotary evaporator. The crude product was precipitated by adding the concentrated residue to ice-cold concentrated hydrochloric acid, which crystallized the sulfonamide intermediate. The precipitated product was collected by filtration and washed with *n*-hexane to remove any remaining organic impurities. The intermediate compound was yielded as pale-brownish crystals via recrystallization [R_f = 0.6, hexane: ethyl acetate (6:4), 1.2175 g, 71.0%], mp 166 − 168 °C. ^{1}NMR 500 MHz (acetone-d_6) δ: 8.03−8.01 (d, J = 8.3 Hz, 2H, H-6, H-4), 7.88−7.86 (d, J = 8.8 Hz, 2H, H-1, H-3), 7.83−7.81 (d, J = 8.3 Hz, 2H, H-17, H-19), 7.24−7.22 ppm (d, J = 8.8 Hz, 2H, H-20, H-16).^{13}C NMR 125 MHz (methanol-d_4) δ: 197.8 (C-21), 143.4 (C-5), 142.0 (C-15), 133.9 (C-18), 132.8 (C-2), 129.7 (C-17, C-19), 127.6 (C-4, C-6), 126.0 (C-7), 124.4 (C-1, C-3), 118.7 (C-16, C-20), 25.0 ppm (C-22); DI-MS (EI): m/z found for $C_{15}H_{12}F_3NO_3S$ is 343.0 [M^+].

2.6.3. General Procedure for the Synthesis of Final Sulfonamide-Chalcones. The sulfonamide-chalcones (compounds **19**, **20**, and **21**) were synthesized via a solvent-free, one-pot Claisen−Schmidt condensation. In this reaction, the intermediate from the first step (1.5 mmol) was mixed with substituted benzaldehydes (3 mmol) in a molar ratio of 1:2 using pelletized sodium hydroxide (NaOH, 2 equiv) as a basic catalyst. The mixture was ground in a mortar for 20−30 min and the reaction progress was monitored by TLC. The resulting crude products were then worked up by dissolving in cold water and subsequent recrystallization from cold methanol. Further purification was performed by column chromatography (hexane: ethyl acetate) and additional recrystallization using various solvent systems. The structure of the final compounds was characterized by ^{1}H and ^{13}C NMR, DI-MS, and FT-IR. All compounds were confirmed to be >95% pure by ^{1}H NMR and GC-MS analyses, with no detectable impurities. The corresponding 1H and 13C NMR, FTIR and DI-MS spectra can be found in Figures S7−S21 in the Supporting Information.

*2.6.3.1. 4-(Trifluoromethyl)-N-(4-(3-(3-(trifluoromethyl)-phenyl)acryloyl)phenyl)benzenesulfonamide (Compound **19**).* Compound **19** was synthesized according to the general procedure using intermediate compound (0.6887 g, 2.0 mmol) and 3-trifluoromethylbenzaldehyde (505.4 μL; 4 mmol). Purification through column chromatography and recrystallization (ethanol: water) yielded the compound as pale orange powder [R_f = 0.76, hexane:ethyl acetate (8:2), 0.050 g, 5.0%], mp 170−172 °C. ^{1}NMR 500 MHz (methanol-d_4) δ: 8.06−8.04 (t, J = 3.2 Hz, J = 12.4 Hz, 2H, H-30, H-24), 8.02−8.00 (d, J = 8.6 Hz, 2H, H-4, H-6), 7.89−7.87 (d, J = 8.6 Hz, 2H, H-1, H3), 7.84−7.83 (d, J = 7.8 Hz, 2H, H-17, H-19), 7.80−

https://doi.org/10.1021/acsomega.5c04809
ACS Omega 2025, 10, 55325−55353

7.77 (d, J = 15.6 Hz, 1H, H-22), 7.72−7.71 (d, J = 7.80 Hz, 1H, H-28), 7.65−7.62 (t, J = 7.8 Hz, 1H, H-26), 7.31−7.29 (d, J = 8.6 Hz, 2H, H-27, H-20), 7.24−7.23 ppm (d, J = 8.6 Hz, 2H, H-16, H-20). ^{13}C NMR 125 MHz (methanol-d_4) δ: 195.7 (C-21), 141.9 (C-5), 141.6 (C-24), 137.2 (C-15), 133.9 (C-25), 133.3 (C-2), 130.2 (C-18), 129.9 (C-29), 129.8 (C-26), 128.2 (C-27), 128.0 (C-17, C-19), 126.5 (C-4, C-6), 125.8 (C-28), 123.7 (C-7), 119.1 (C-1, C-3), 119.0 (C-16, C-20), 117.3 (C-30), 115.5 (C-31), 104.5 ppm (C-22); FTIR: 3128.50 (N−H stretch), 2918.76 and 2851.27, (CH aromatic and C═C−H alkene), 1730.49, (C═O ketone), 1655.64 and 1580.36 (C═C aromatic), 1599.10 (C═C alkene) and 1510.89 cm^{-1} (N−H bend); DI-MS (EI): m/z found for $C_{23}H_{15}F_6NO_3S$ is 499.0 [M^+].

*2.6.3.2. 4-(Trifluoromethyl)-N-(4-(3-(4-(trifluoromethyl)-phenyl)acryloyl)phenyl)benzenesulfonamide (Compound **20**).* Compound **20** was synthesized according to the general procedure using intermediate compound (0.6887 g, 2.0 mmol) and 4-trifluoromethylbenzaldehyde (0.6964 g; 4 mmol). Purification through column chromatography and recrystallization (methanol: water) yielded the compound as an orange powder [R_f = 0.70, hexane:ethyl acetate (8:2), 0.110 g, 11.0%], mp 206−208 °C. ^{1}NMR 500 MHz (methanol-d_4) δ: 8.06−8.05 (d, J = 8.4 Hz, 2H, H-6, H-4), 8.04−8.02 (d, J = 8.8 Hz, 2H, H-1, H-3), 7.93−7.91 (d, J = 8.1 Hz, 1H, H-24), 7.89−7.87 (d, J = 8.4 Hz, 2H, H-27, H-29), 7.84−7.83 (d, J = 8.00 Hz, 2H, H-17, H-19), 7.79−7.76 (d, J = 15.7 Hz, 1H, H-22), 7.31−7.30 (d, J = 8.9 Hz, 2H, H-26, H-30), 7.25 − 7.23 ppm (d, J = 8.5 Hz, 2H, H-16, H-20). ^{13}C NMR 125 MHz (methanol-d_4) δ: 195.6 (C-21), 146.3 (C-5), 143.6 (C-24), 141.6 (C-15), 133.7 (C-25), 133.7 (C-2), 133.3 (C-18), 130.2 (C-27, C-29), 124.4 (C-7, C-31), 119.1 (C-1, C-3), 119.0 (C-16, C-20), 113.9 ppm (C-14); FTIR: 3123.76 (N−H stretch), 2924.92 and 2868.66, (CH aromatic and C═C−H alkene), 1686.89 (C═C alkene), 1655.68 (C═O ketone), 1599.08 and 1513.31 (C═C aromatic), 1474.55 cm^{-1} (N−H bend); DI-MS (EI): m/z found for $C_{23}H_{15}F_6NO_3S$ is 499.0 [M^+].

*2.6.3.3. N-(4-(3-(4-Bromophenyl)acryloyl)phenyl)-4-(trifluoromethyl)benzenesulfonamide) (Compound **21**).* Compound **21** was synthesized according to the general procedure using intermediate compound (0.515 g; 1.5 mmol) and 4-bromobenzaldehyde (0.5550 g; 3 mmol). Purification through column chromatography and recrystallization (ethanol: water) yielded the compound as pale-yellowish crystals [R_f = 0.70, hexane: ethyl acetate (6:4), 0.124 g, 16.2%], mp 180−182 °C.^{1}NMR 500 MHz (acetone-d_6) δ: 8.14−8.12 (d, J = 8.4 Hz, 2H, H-6, H-4), 8.10−8.09 (d, J = 8.8 Hz, 2H, H-1, H-3), 7.96−7.94 (d, J = 8.4 Hz, 2H, H-17, H-19), 7.88−7.85 (d, J = 15.7 Hz, 1H, H-22), 7.78−7.77 (d, J = 8.5 Hz, 2H, H-27, H-29), 7.72−7.69 (d, J = 15.7 Hz, 1H, H-24), 7.64−7.62 (d, J = 8.5 Hz, 2H, H-30, H-26), 7.42−7.40 ppm (d, J = 8.8 Hz, 2H, H-20, H-16). ^{13}C NMR 125 MHz (methanol-d_4) δ: 189.0 (C-21), 143.4 (C-5), 143.0 (C-24), 142.1 (C-15), 133.2 (C-25), 134.0 (C-2), 133.5 (C-18), 131.8 (C-27, C-29), 130.0 (C-26, C-30), 129.9 (C-17, C-19), 127.6 (C-4, C-6), 126.0 (C-7), 124.4 (C-28), 124.3 (C-1, C-3), 122.0 (C-16, C-20), 118.8 ppm (C-22); FTIR 3328.70 (N−H stretch), 2918.67 and 2850.29 (CH aromatic and C═C−H alkene), 1650.94 (C═O ketone), 1605.33 (C═C alkene), 1593.86 and 1510.39 (C═C aromatic), 1485.88 ppm (N−H bend); DI-MS (EI): m/z found for $C_{22}H_{15}BrF_3NO_3S$ is 511.0 [M^+].

2.7. Zebrafish In Vivo Assays. *2.7.1. Zebrafish Husbandry and Breeding.* All experiments with wild-type (WT) zebrafish were approved by the Institutional Animal Care and Use Committee (IACUC) of the Animal Ethics Committee of Universiti Putra Malaysia (IACUC-R024/2023). WT zebrafish aged >6 months were maintained in 2-L aquaria with reverse osmosis (RO) in a 14-h light/10-h dark cycle at 25−27 °C and pH 7.0−7.5. The fish were kept in a 2:3 male-to-female ratio in a single tank to provide a stress-free environment and were fed brine shrimp (*Artemia salina*) 3 to 4 times per day. Zebrafish embryos were obtained by mating adult WT zebrafish using standard methods. Fertilized eggs were collected from the mating medium and rinsed with embryo medium (EM). All larvae were reared in the same embryo medium and in the same Petri plate to control the variation of incubation conditions until the day of assessment. The medium was renewed every day and mortality was monitored every 24 h until 7 days postfertilization (dpf).

2.7.2. Evaluation of the Mortality Rate of Zebrafish Embryos. 2.7.2.1. Dose Selection and Validation. In this study, five concentrations (0, 3.13, 6.25, 12.5, and 25 μM) of compounds **19**, **20**, and **21** were selected based on a 2-fold serial dilution, starting with 25 μM as the highest dose. This approach allowed a systematically evaluation of the effects of the compounds over a relevant dose range. All concentrations were prepared by serial dilution from 100 mM stock solutions. Specifically, 0.0101, 0.0103, and 0.0100 g of compounds **19**, **20**, and **21** were dissolved in 202, 203, and 196 μL of DMSO, respectively.

2.7.2.2. Experimental Protocol. Healthy WT zebrafish embryos at 5 h postfertilization (hpf) were exposed to each concentration, including a control group. Embryos were gently rinsed and transferred to clean Petri dishes containing embryo medium to remove debris and waste prior to treatment. The experiment was performed in triplicate, with 10 embryos per well in 24-well plates (total n = 30 per concentration). Each well was treated by immersion with 2000 μL of the respective test compound. Mortality was monitored and recorded daily, and the LC_{50} value was determined at 120 hpf. All observations were performed using a Leica EZ4W stereomicroscope (Leica Microsystems GmbH, Wetzlar, Germany).

2.7.3. Locomotor Activity in Zebrafish Epilepsy Model. 2.7.3.1. PTZ Seizure Induction and Validation. At 6 dpf, zebrafish larvae (n = 6 per group) were individually placed in the wells of a 24-well plate (n = 1 larvae/well), each containing 2000 μL of embryo medium, and allowed to acclimate. The locomotor behavior was recorded using an iPhone 15 ProMax camera with a 48-megapixel (MP) sensor, 60 fps, mounted directly above the observation chamber. At 7 dpf, WT larvae were exposed to 2.5 mM PTZ for 10 min to induce epileptiform activity. This PTZ concentration was validated by preliminary dose−response studies (2.5, 5.0, 6.0, and 10.0 mM) to determine the optimal concentration that reliably induces stage III−IV seizures (Table 3) in larvae while maintaining mortality.

2.7.3.2. Seizure Scoring Systems. Following induction, larvae were treated with compounds **19**, **20**, **21**, and VPA (positive control; 100 μM),[46] and acclimatized for 1 h prior to behavioral assessment. The total observation time for locomotor activity was 10 min, and movement was measured in cm/s. All raw video recordings were exported, and behavioral trajectories were analyzed using the Animal Tracker plugin in ImageJ software (National Institutes of Health, Maryland, USA). Seizure-like behavior was scored using a previously published seizure behavior scoring system,[47] as

https://doi.org/10.1021/acsomega.5c04809
ACS Omega 2025, 10, 55325−55353

Table 3. Zebrafish Seizure Scoring Systems

scoring of zebrafish seizure behavior[a]	seizure stage
at rest or short swimming at the bottom of the tank	0
increased in swimming frequency and gill cover movement	I
sudden bursts of locomotion, whirlpool-like swimming	II
repetitive circular movements and rapid movements	III
rhythmic muscle contractions resembling clonus-like behavior	IV
sinking to the bottom of the tank, resembling tonic-like seizures	V

[a]Seizure scoring was defined according to Baraban et al.[47]

shown in Table 3. Behavioral end points, including total freezing duration (s), total distance traveled (cm), total speed traveled (cm/s) and total acceleration (cm/s^2).

2.7.3.3. Statistical Analysis. All obtained results were calculated as mean ± standard error mean (SEM) using GraphPad Prism 9.3.0 (San Diego, CA, USA). Normality test was performed before conducting one-way analysis of variance (ANOVA) for toxicity profile and antiepileptic behavioral effect to obtain *p*-values, followed by Tukey's post hoc test. $p \leq 0.05$ was considered a significant difference from the other treatment groups. Pearson's correlation was used to assess the correlation between the total freezing count and locomotion (total speed measured) for the PTZ-induced groups treated with compounds **19**, **20**, and **21** (PTZ + compound **19**; PTZ + compound **20**; and PTZ + compound **21**).

3. RESULTS AND DISCUSSION

3.1. Physicochemical and ADMET Prediction. Drug likeness is a qualitative method used in drug discovery and development to assess the extent to which a newly designed substance resembles approved FDA drugs in terms of its bioavailability and oral absorption, based on its structural and physicochemical characteristics.[48,49] The well-known RO5 is applied to predict the absorption or permeability of potential drug candidates through lipid bilayers in the human body.[50] A compound is classified as likely bioavailable if it meets the criteria of the RO5 (Pfizer) in combination with the Veber rule (GSK) and the EGAN rule (Pharmacia), as shown in Table 4. The identified drug-like properties can also be visualized using a bioavailability radar, as depicted in Figure 4. The results show that the intermediate 4-aminochalcones (series I) and most sulfonamide-containing chalcones (series II and III) fully fulfill the criteria for drug-like properties, except for compounds **13**, **14**, **15**, **16**, and **31** (log*P* > 5).

In particular, the log*P* value serves as a key indicator of the lipophilicity properties of compounds as prospective medications, with adequate log*P* < 5 being essential. It is crucial to analyze log*P*, as log*P* predicts solubility, absorption, membrane penetration, plasma protein binding, distribution, tissue penetration, and ligand transport to molecular targets.[51] Higher log*P* values suggest stronger lipophilicity and likely poorer solubility in water. Excessive lipophilicity (log*P* > 5) often leading to increased metabolic turnover, limiting bioavailability and maximum absorbable dose. In addition, highly lipophilic compounds tend to bind nonspecifically to other hydrophobic sites of molecular targets, increasing the likelihood of promiscuity and toxicity.[52]

Although several Series II sulfonamide-chalcones meet or exceed the Lipinski molecular weight (M_W) threshold of 500 Da, the MW alone is an unreliable predictor of oral bioavailability or permeability. Veber et al. demonstrated that compounds with ≤10 rotatable bonds and a total polar surface area (TPSA) ≤ 140 Å^2 generally have good membrane permeability and oral absorption.[53] All Series II compounds fulfill the Veber criteria (7−9 rotatable bonds, TPSA 71.62−80.85 Å^2), and placing them within the "extended Rule of Five" range, which includes clinically successful drugs.[54] Notably, CNS drugs, such as lurasidone (M_W = 529 Da) exceed the Lipinski's M_W limit yet retain high oral bioavailability and effective BBB penetration, when other physicochemical properties (low hydrogen bond counts, moderate lipophilicity, and optimal TPSA) are maintained. Series II compounds similarly exhibited high human intestinal absorption (HIA; 76.0−79.6%) and strong BBB penetration (89.7−97.3%), supporting their CNS potential despite a higher M_W.[55,56] These findings reflect trends in modern CNS drug discovery, where 500−600 Da compounds succeed when TPSA and molecular flexibility are optimized.[57,58]

This relationship between lipophilicity (log*P*) and solubility (log*S*) underscores a significant challenge for the pharmaceutical industry, as approximately 50% of marketed drugs and nearly 90% of molecules in the pipeline are poorly water-soluble. To address this challenge, log*S* was calculated using the ESOL data set to predict gastrointestinal (GI) absorption potential.[59] As shown in Table 4, the sulfonamide-chalcones analyzed with log*S* greater than −3 demonstrated good solubility; those with log*S* between −4 and −6 showed moderate solubility, except for compounds **19**, **20**, and **21**, which displayed poor solubility (log*S* > −6), indicating significant potential challenges in formulation. These findings are aligned with the General Solubility Equation (GSE)[60] which emphasizes the inverse relationship between log*P* and log*S*. Oral administration of poorly water-soluble drugs is often problematic due to their limited dissolution in GI fluids, which impairs intestinal absorption, reduces systemic exposure and results in insufficient therapeutic effect.[61] Similarly, intravenous (IV) administration of poorly soluble drugs often requires higher amounts of solubilizers (cosolvents, surfactants), which often cause adverse reactions such as hemolysis and hypersensitivity.[61,62] Despite these problems, successful formulation strategies have enabled the commercialization of several AEDs. For instance, carbamazepine, with a solubility of less than 200 μg/mL remains a first-line AEDs and has achieved clinical success through formulation enhancements such as cyclodextrin complexation with 2-hydroxypropyl-β-cyclodextrin (for IV administration), solid dispersions with polyethylene glycols (PEG-4000, PEG-6000, PEG-8000), and spray-dried surfactants systems.[63] As shown in Supplementary Table S2, absorption prediction analysis shows that most sulfonamide-chalcones have high GI absorption, except for Series II compounds and Series III compounds **31**−**32**. Their lower absorption potential is likely due to high molecular weight, poor solubility, and increased TPSA.[59] While log*S* has less direct influence on the BBB model than log*P*, poor solubility can indirectly affect drug metabolism and pharmacokinetics through its impact on bioavailability. Therefore, addressing solubility at an early stage of drug development is essential, as poor solubility is one of the main causes of clinical failures. Our results underpin this challenge and will inform future optimization and formulation strategies to improve the clinical usability of these sulfonamide-chalcone compounds.

Meanwhile, PAINS are substances with reactive structural cores that cause false-positive bioactivity results. This can occur through various mechanisms, including colloidal

https://doi.org/10.1021/acsomega.5c04809
ACS Omega 2025, 10, 55325−55353

Table 4. Physicochemical Properties, PAINS, Aggregation, and Other Properties in the Determination of Drug-like Characteristics of Newly Designed Aminated- and Sulfonamide-Containing Chalcones (Compounds 1−36), Calculated with the FAF-Drugs4, SwissADME, and ChemAG

compound	M_W (g/mol)	log*P*	water solubility		HBD	HBA	ROS violation	NRB	TPSA (Å^2)	oral bioavail-ability (VEBER)	oral bioavail-ability (EGAN)	PAINS	aggregator probability	PLD	Fsp^3
			log*S* (ESOL)	class											
series I															
1	223.27	2.40	−3.060	soluble	2	2	0	3	43.09	good	good	no	0.101	NI[a]	0.00
2	253.30	3.25	−3.66	soluble	2	3	0	4	52.32	good	good	no	0.148	NI[a]	0.06
3	253.30	3.23	−3.65	soluble	2	3	0	4	52.32	good	good	no	0.163	NI[a]	0.06
4	241.26	3.32	−3.72	soluble	2	2	0	3	43.09	good	good	no	0.225	NI[a]	0.00
5	241.26	3.23	−3.67	soluble	2	2	0	3	43.09	good	good	no	0.073	NI[a]	0.00
6	241.26	2.50	−3.21	soluble	2	2	0	3	43.09	good	good	no	0.085	NI[a]	0.00
7	291.27	4.01	−4.33	moderately soluble	2	2	0	4	43.09	good	good	no	0.062	NI[a]	0.06
8	291.27	3.28	−3.87	soluble	2	2	0	4	43.09	good	good	no	0.049	NI[a]	0.06
9	302.17	3.09	−3.96	soluble	2	2	0	3	43.09	good	good	no	0.358	NI[a]	0.00
10	257.71	3.03	−3.64	soluble	2	2	0	3	43.09	good	good	no	0.189	NI[a]	0.00
11	259.25	3.21	−3.74	soluble	2	2	0	3	43.09	good	good	no	0.050	NI[a]	0.00
12	259.25	3.35	−3.74	soluble	2	2	0	3	43.09	good	good	no	0.050	NI[a]	0.00
series II															
13	431.43	**5.10**[c]	−5.71	moderately soluble	1	6	1	7	71.62	good	good	no	0.370	NI[a]	0.05
14	461.45	**5.07**[c]	−5.78	moderately soluble	1	7	1	8	80.85	good	good	no	0.699	NI[a]	0.09
15	461.45	**5.07**[c]	−5.78	moderately soluble	1	7	1	8	80.85	good	good	no	0.513	NI[a]	0.09
16	449.42	**5.20**[c]	−5.87	moderately soluble	1	7	1	7	71.62	good	good	no	0.638	NI[a]	0.05
17	449.42	**5.20**[c]	−5.87	moderately soluble	1	7	1	7	71.62	good	good	no	0.492	NI[a]	0.05
18	449.42	**5.20**[c]	−5.87	moderately soluble	1	7	1	7	71.62	good	good	no	0.301	NI[a]	0.05
19	499.43	**5.98**[c]	−6.57	**poorly soluble**[d]	1	9	1	8	71.62	good	good	no	0.475	NI[a]	0.09
20	499.43	**5.98**[c]	−6.57	**poorly soluble**[d]	1	9	1	8	71.62	good	good	no	0.211	NI[a]	0.09
21	**510.32**[b]	**5.79**[c]	−6.62	**poorly soluble**[d]	1	6	2	7	71.62	good	good	no	0.586	NI[a]	0.05
22	465.87	**5.73**[c]	−6.31	**poorly soluble**[d]	1	6	1	7	71.62	good	good	no	0.437	NI[a]	0.05
23	467.41	**5.30**[c]	−6.03	**poorly soluble**[d]	1	8	1	7	71.62	good	good	no	0.332	NI[a]	0.05
24	467.41	**5.30**[c]	−6.03	**poorly soluble**[d]	1	8	1	7	71.62	good	good	no	0.338	NI[a]	0.05
series III															
25	393.46	3.96	−4.79	moderately soluble	1	5	0	6	80.85	good	good	no	0.664	NI[a]	0.05
26	423.48	4.16	−5.00	moderately soluble	1	6	0	7	**90.08**[e]	good	good	no	0.812	NI[a]	0.09
27	423.48	3.93	−4.86	moderately soluble	1	6	0	7	**90.08**[e]	good	good	no	0.613	NI[a]	0.09
28	411.45	4.29	−5.09	moderately soluble	1	5	0	6	80.85	good	good	no	0.853	NI[a]	0.05

https://doi.org/10.1021/acsomega.5c04809
ACS Omega 2025, 10, 55325−55353

Table 4. continued

compound	M_W (g/mol)	log*P*	water solubility		HBD	HBA	ROS violation	NRB	TPSA (Å^2)	oral bioavail-ability (VEBER)	oral bioavail-ability (EGAN)	PAINS	aggregator probability	PLD	Fsp^3
			log*S* (ESOL)	class											
series III															
29	411.45	4.29	−5.09	moderately soluble	1	5	0	6	80.85	good	good	no	0.809	NI[a]	0.05
30	411.45	4.06	−4.95	moderately soluble	1	5	0	6	80.85	good	good	no	0.744	NI[a]	0.05
31	461.46	**5.07**[c]	−5.78	moderately soluble	1	5	1	7	80.85	good	good	no	0.755	NI[a]	0.09
32	461.45	4.84	−5.64	moderately soluble	1	5	0	7	80.85	good	good	no	0.513	NI[a]	0.09
33	472.35	4.65	−5.70	moderately soluble	1	5	0	6	80.85	good	good	no	0.820	NI[a]	0.05
34	427.90	4.59	−5.38	moderately soluble	1	5	0	6	80.85	good	good	no	0.758	NI[a]	0.05
35	429.44	4.39	−5.25	moderately soluble	1	5	0	6	80.85	good	good	no	0.743	NI[a]	0.05
36	429.44	4.39	−5.25	moderately soluble	1	5	0	6	80.85	good	good	no	0.663	NI[a]	0.05
AEDs															
VPA	144.21	2.75	−2.14	soluble	1	2	0	5	37.30	good	good	no	0.026	NI[a]	0.88
Topiramate	339.36	−0.83	−1.22	very soluble	1	9	0	3	**123.92**[e]	good	good	no	0.012	NI[a]	1.00

[a]NI (noninducer). [b]M_W > 500 (RO5 violation). [c]log*P* > 5 (RO5 violation). [d]Poorly soluble. [e]TPSA > 90 Å^2.

https://doi.org/10.1021/acsomega.5c04809
ACS Omega 2025, 10, 55325−55353

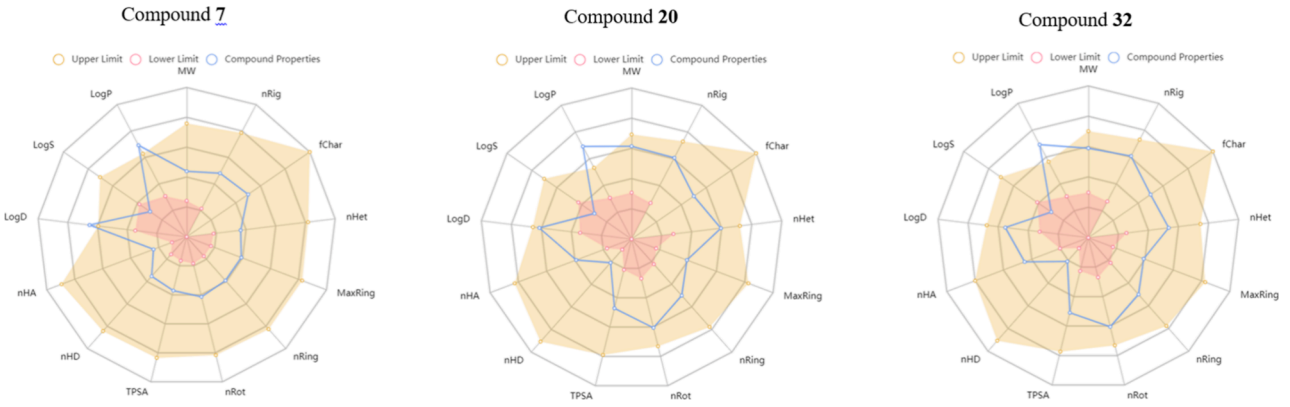

Figure 4. Bioavailability radar for selected amino-chalcone and sulfonamide-chalcones, compound **7** (series I), compound **20** (series II), and compound **32** (series III).

aggregation. Therefore, PAINS and aggregation alerts should ideally be predicted in the early stages of drug development prior to the synthesis step to exclude false hits. The results presented in Table 4 show that the designed sulfonamide-chalcones (compounds **1**−**36**) are non-PAINS and are nonaggregator molecules (aggregator probability <1). In addition, phospholipidosis (PLD) and Fsp^3 are analyzed to predict the solubility of the potential drug. refers to the drug-induced abnormal accumulation of phospholipids and drugs in lysosomes in human organs such as liver, kidney and lung, and can affect cell viability.[64] All chalcones were predicted to be non-PLD inducer, which emphasizes their favorable safety, pharmacology, efficacy, bioavailability, genetic toxicity and pharmacokinetics properties. On the other hand, all compounds **1**−**36** are predicted to have poor solubility as they lack sp^3-hybridized carbon atoms (Fsp^3 values <0.30), as indicated in Table 4.[65]

Subsequently, the pharmacokinetic behavior of the sulfonamide-chalcones was assessed using an in silico ADME approach to predict their absorption (A), distribution (D), metabolism (M), excretion (E), and potential toxicity. Supplementary Table S2 summarizes the ADME properties of compounds **1**−**36**, compared to established AEDs (VPA and topiramate), including HIA, BBB permeability, PPB, and CYP2C19 inhibition. Series I compounds had the highest predicted HIA values (0.782−0.900), comparable to VPA and topiramate, which are known to have approximately 90% bioavailability. In contrast, series II (0.760−0.796) and series III (0.720−0.777) compounds have a lower predicted absorption. Nonetheless, all newly designed compounds showed HIA values between 72.60 and 90%, exceeding the threshold for good intestinal absorption (HIA+: ≥30%). These results indicate that the newly designed compounds possess favorable oral bioavailability potential, as supported by the robust AUC performance of ADMETlab 3.0s and the evidential deep learning-based uncertainty quantification. This is essential for the therapeutic efficacy of AEDs, as they must be absorbed into the bloodstream to exert their effect on the CNS.[66,67]

The BBB is a critical factor in the design and development of CNS therapeutics, and BBB permeability can be systematically categorized as follows: (a) BBB penetration score >2.0 indicates high penetration into the CNS, (b) 0.1 < BBB < 2.0 indicates moderate penetration into the CNS, and (c) BBB permeability <0.1, indicates poor BBB penetration.[68] Series II compounds had BBB penetration values ranging from 0.897 to 0.973, which closely matched the high BBB penetration of VPA (BBB score = 0.99) and topiramate (BBB score = 0.96). Series I showed comparable BBB permeability (0.834−0.971), while Series III showed robust penetration (0.825−0.947). The predictive classification models for BBB permeability achieved an AUC value of 0.90, indicating high reliability. These results support the therapeutic potential of the evaluated compounds, particularly in epilepsy treatment.

Furthermore, all compounds showed a high plasma protein binding affinity (PPB > 90%), which is important since only unbound drugs can cross cell membranes to reach pharmacological targets. AEDs with high PPB tend to have a longer duration of action and slower elimination from the body. Metabolism is another important aspect of drug development, primarily occurring in the liver through cytochrome P450 isoenzymes and can influence the toxicity, efficacy and adverse effects of drugs.[69] Of the six major cytochrome P450 isoenzymes (CYP1A2, CYP2C19, CYP2C9, CYP2D6, CYP2E1 and CYP3A4),[70] only CYP2C19 was investigated in this study. All compounds were identified as CYP2C19 inhibitors (AUC = 0.89), which may decrease drug metabolism and increase plasma concentrations, potentially beneficial for overcoming pharmacoresistance.[71,73] However, CYP2C19 inhibition also poses a significant risk for drug−drug interactions (DDIs), particularly in the treatment of epilepsy, where 30−40% of patients require polytherapy with multiple AEDs.[72] This dual importance highlights the need for careful dose adjustment, therapeutic drug monitoring, and comprehensive pharmacokinetic evaluation to optimize efficacy while minimizing the risks of drug−drug interactions during clinical development.

P-glycoprotein (PgP) plays a central role in the regulation of drug transport across the BBB and influences both the pharmacokinetics and CNS exposure of AEDs. In contrast to VPA, which only minimally inhibits CYP and PgP, all three sulfonamide-chalcone series, with the exception of certain series I compounds, inhibit both CYP2C19 and PgP according to ADMETlab 3.0. PgP inhibition may improve brain uptake and therapeutic efficacy by reducing drug efflux at the BBB.[74] However, PgP inhibition presents dual implications. While it can improve the bioavailability and CNS penetration of AEDs, it also increases the risk of neurotoxicity by facilitating the accumulation of neurotoxic substances in the brain. For example, PgP-deficient mice show a 100-fold increase in brain uptake of ivermectin,[75] and coadministration of tariquidar with fentanyl significantly increases CNS exposure and induces

https://doi.org/10.1021/acsomega.5c04809
ACS Omega 2025, 10, 55325−55353

respiratory toxicity.[76] In addition, PgP inhibition can lead to clinically significant DDIs, particularly with co- administered PgP substrates, such as verapamil, quinidine and dronedarone, which can increase systemic drug levels and increase the risk of adverse events.[77] Therefore, early screening and comprehensive pharmacological evaluation of both CYP2C19 and PgP inhibition are essential to optimize the benefit-risk− profile and enable safe and effective AED development.

Following the ADME analysis, all designed sulfonamide-chalcones were subjected to in silico toxicity prediction, which included assessment of genotoxicity, drug-induced neurotoxicity, respiratory toxicity, skin sensitization, rat toxicity, AMES mutagenicity, and carcinogenicity to prioritize the compounds with minimal or no predicted toxic liabilities (Supplementary Tables S3 and S4). Among these end points, genotoxicity is particularly critical in the context of epilepsy treatment during pregnancy, as approximately 10% of affected pregnancies are associated with congenital defects attributable to genotoxic effects.[78] Similarly, neurotoxicity, a common adverse effect of antiepileptic drugs (AEDs), was assessed using probability scores generated by the ADMETlab platform, with values between 0.7−1.0 indicating high risk and 0−0.3 indicating low risk. Respiratory toxicity was also assessed, including the potential for irritation, inflammation or impaired lung function. The prediction results showed that the intermediate 4-aminochalcones (**1**−**12**) had a potential risk of genotoxicity, neurotoxicity and respiratory toxicity. In contrast, the sulfonamide-chalcones of series II and III (compounds **13**−**36**) showed no such toxic properties. It is noteworthy that series II and III, which contain sulfonamide moieties, also showed no predicted skin sensitization. This can be attributed to the intrinsic anti-inflammatory properties of sulfonamides, which supports their potential suitability for topical formulations. In addition, the AMES mutagenicity test categorized all sulfonamide-containing chalcones in series II and III as nonmutagenic, alleviating concerns regarding carcinogenic potential. Carcinogenicity, defined as the potential of a substance to cause cancer, is an important consideration when assessing drug safety. Series II and III were predicted to have good safety profiles that directly address some of the most serious limitations of current AED therapies. While VPA is associated with well-documented risks, such as teratogenicity, hepatotoxicity (including potentially fatal liver failure),[79] and carcinogenic potential, and topiramate poses significant teratogenic risks, such as oral clefts (2.2% incidence, 11-fold higher than in the baseline population),[80] both Series II and III compounds are predicted as nonmutagenic. In addition, Series II is further classified as noncarcinogenic, underscoring its better safety profile relative to existing AEDs. In this study, only compounds **7** and **8** of Series I were classified as noncarcinogenic, which may be related to the presence of trifluoromethylbenzene, a substituent that may have a protective effect. The fact that the Series II compounds were not predicted to be carcinogenic emphasizes the role of the sulfonamide groups in reducing cancer risk. However, the varied carcinogenic potential of the Series III compounds highlights the influence of specific structural modifications and substituents and emphasizes the need for further studies to clarify their mechanistic effects.

In this study, all predicted toxicities of Series I (**1**−**12**) were primarily associated with the 4-amino group. This functionality is a known structural alert for toxicity, as *N*-hydroxylation can occur by cytochrome P450, producing arylhydroxylamine intermediates that are auto-oxidized to reactive nitroso compounds.[81,82] These species can bind covalently to cellular macromolecules, including DNA (formation of mutagenic DNA adducts leading to genotoxicity)[83] and proteins (formation of immunogenic haptens by cysteine residues adduction),[84] as well as blood protein modifications,[85] demonstrating the covalent binding potential of nitroso metabolites. In addition, the electron-donating nature of the amino group may compromise metabolic stability and increase its susceptibility to bioactivation to toxic metabolites. Conversion of the weak electron-withdrawing amino group to a stronger sulfonamide moiety successfully eliminated predicted toxicities at all end points, highlights the importance of strategic chemical modifications in improving safety profiles. The resulting sulfonamide-containing chalcones (Series II and III) showed good ADMET properties, with Series II compounds exhibiting the most favorable pharmacokinetic and toxicological profiles. These findings underscore the potential of sulfonamide derivatives as safer and more effective AED candidates that offer advantages over existing AEDs by addressing key therapeutic limitations while maintaining their efficacy.

3.2. Molecular Docking. Before the selected ligand-protein complexes were submitted for MD, all newly designed compounds (**1**-**36**) were first molecularly docked to the $GABA_A$ target to determine the binding affinity and intermolecular interactions in prioritizing promising GABA antagonists among the compounds. The neurotransmitter binding pocket of $GABA_A$Rs is located between the extracellular domains (ECDs), between the 'principal' face (loops A−C) and the 'complementary' face (loops D and E) (Supplementary Figure S1).[36] During molecular docking, the orthosteric GABA binding site at the β^+/α^- subunit of the $GABA_A$ receptor was targeted, which is oriented toward the benzamidine cocrystallized structure (PDB: 4COF). This site was chosen to reflect the native GABA binding domain and is supported by literature indicating that chalcone and sulfonamide derivatives may exert modulatory effects through interactions within or in proximity to the orthosteric cleft.[86,87] Docking analysis revealed that the active site of $GABA_A$Rs consists of Asp 95−Leu 99 (loop A), Glu 155−Tyr 159 (loop B), and Phe 200−Tyr 205 (loop C) from the 'principal' face and the 'complementary' face Tyr 62−Gln 64 and Leu 125−Arg 129 from loops D and E, respectively.[88] In general, the molecular docking strategy was validated by redocking the cocrystallized benzamidine in the $GABA_A$ receptor. The binding affinity and RMSD values of the redocked benzamidine were determined to be −6.7 kcal/mol and 0.6835 Å, respectively. The RMSD value <2.0 Å was considered acceptable,[89] indicating that the predicted binding mode closely matches the conformation found in the published X-ray crystallography. As shown in Supplementary Figure S2, the redocked conformation of benzamidine with the highest docking score is closely overlaps with its cocrystallized pose, and both molecules exhibit a similar torsional orientation, confirming the accurate pose reproduction. More importantly, the ROC-AUC analysis yielded an outstanding virtual screening performance with an AUC value of 0.996 (Supplementary Figure S3), well above the typical AUC values for success thresholds of 0.65−0.90.[90,91] This near-perfect discrimination ability corresponds to a 99.6% probability that a randomly selected active compound will be ranked higher than a decoy. The enrichment factors, EF1%

https://doi.org/10.1021/acsomega.5c04809
ACS Omega 2025, 10, 55325−55353

(29.00) and EF5% (21.75) are further evidence of the early detection performance of the protocol. They reflect a 29- and 21.75-fold enrichment compared to random selection. These enrichment values exceed literature benchmarks, where EF1% values of 10−20 are considered excellent.[90,91] Finally, the use of empirically based cut-offs anchored to benzamidine (−6.7 kcal/mol) and VPA (−5.4 kcal/mol) provides a target-specific, reproducible criterion for hit selection. The convergence of the geometric (RMSD) and statistical (ROC-AUC and enrichment factors) validations provides orthogonal evidence for the reliability and predictive accuracy of the molecular docking used in this study.

Table 5 presents the top three trifluoromethylsulfonamide-containing chalcones (compounds **19**, **20**, and **21** from Series II) that exhibited the most stable interactions with the allosteric site of the $GABA_A$ receptor, with docking values of −10.3, −10.3, and −10.1 kcal/mol, respectively. In contrast, other compounds showed weaker binding affinity, indicating lower stability (Supplementary Table S5). These results emphasize the improved interaction stability of the newly designed chalcones with the $GABA_A$ receptor, which is primarily due to H-bonding.

Table 5. Binding Affinity and Selected Binding Interactions (Hydrogen and Halogen Bonds) of the Newly Designed Sulfonamide-Chalcones (Compounds 19−21) and Sodium Valproate (VPA) with the Active Site Residue of the $GABA_A$ Receptor[a]

		protein−ligand interactions			
compound	binding affinity (kcal/mol)	ligand	receptors	interactions	bonding distance (Å)
19	−10.3	N−H	Ala45	H-bond	2.2
		−F	Glu155	halogen (F)	2.81
		−F	Tyr157	halogen (F)	2.82
		−F	Tyr97	H-bond	2.95
		−F	Asp48	halogen (F)	2,98
		−F	Tyr157	halogen (F)	3.18
		−F	Glu155	halogen (F)	3.45
		−F	Ser156	halogen (F)	3.64
		−F	Ile47	halogen (F)	3.68
20	−10.3	−F	Thr151	H-bond	2.21
		−F	Thr202	H-bond	2.28
		−F	Met137	H-bond	2.66
		−F	Tyr157	halogen (F)	3.16
		−F	Ala135	halogen (F)	3.18
		−F	Tyr157	halogen (F)	3.19
		−F	Asn149	halogen (F)	3.55
21	−10.1	N−H	Ala45	H-bond	2.2
		−F	Asn100	C−H bond	3.23
		−F	Asp48	C−H bond	3.41
		−F	Glu182	halogen	3.53
VPA	−5.4	−O−H	Thr202	H-bond	2.55
		−F	Tyr97	H-bond	3.27
		−F	Glu155	halogen (F)	3.46

[a]H-bond: Hydrogen bonding.

Supplementary Figure S4a−f and Figure 5a−c depict the 3D and 2D binding interactions of potentially active sulfonamide-chalcones **19**, **20**, and **21** with the active center of the $GABA_A$ receptor. These compounds show similar interactions with important amino acid residues as the reference drug VPA. Docking analysis revealed that these compounds **19**, **20**, and **21** adopt stable poses within the orthosteric GABA binding site at the β^+/α^- subunit interface and bind the residues of loops A−E via H-bonds, halogen bonds, and hydrophobic interactions. Compound **19** forms H-bonds with Ala45 (2.20 Å) and Tyr97 (2.95 Å), which are known to enhance ligand specificity and reduce conformational mobility within the pocket. Compound **19** also forms halogen bonds with Glu155, Asp48, Ser156, Ile47, and Tyr157, as well as a σ-hole on the fluorine, which contributes to additional electrostatic stabilization, increased binding affinity, and specificity.[92] Compound **20** forms hydrogen bonds with Thr202 (2.28 Å), Thr151 (2.21 Å), and Met137 (2.66 Å) and halogen bonds with Tyr157, Ala135, and Asn149. Meanwhile, compound **21** forms a hydrogen bond with Ala45 (2.20 Å) and two C−H interactions with fluorine substituents. Hydrophobic interactions were also observed with Tyr62, Tyr205, Leu99, and Ala135 for compound **19**, with Tyr62, Phe200, Tyr205, Ala45, and Leu99 for compound **20**, and with Ala135, Leu99, Tyr205, Phe200, and Tyr62 for compound **21** (Figure 5a−c). These results, which are summarized in Table 5, highlight the strong receptor−ligand interactions of these sulfonamide-chalcones. For all three ligands, $\pi-\pi$ stacking and π−alkyl interactions with Tyr62 (loop D), Phe200 and Tyr205 (loop C), Leu99 (loop A), and Ala135 (loop E) stabilize binding by connecting to aromatic box of the $GABA_A$ receptor. The planar, conjugated chalcone scaffold optimally positions its aromatic rings for these interactions, enhancing both binding affinity through London dispersion forces and binding selectivity by fitting the unique geometry of the $GABA_A$ aromatic cleft. The detailed overall binding interactions of these compounds with the receptor are summarized in Table 6.

The superiority of compound **20** over compounds **19** and **21** is primarily due to the two *para*-CF_3 substituents on the sulfonamide and chalconoid rings, which increase lipophilicity by ∼0.7 log*P* units and thus facilitate BBB penetration. In addition, the strong electron-withdrawing induction effect of CF_3 (σ_p = +0.54) lowers the NH pK_a of the sulfonamide, strengthening hydrogen bonding at Thr151 and Thr202. This inductive effect also polarizes the π system of the chalcone, increases the molecular dipole moment and strengthens the electrostatic control in the orthosteric cleft.

3.3. Fragment-Based SAR of CYP2C19 Inhibitors.

Based on the promising molecular docking results and the favorable ADMET profiles, including predictions for CYP2C19 interactions (Supplementary Table S3), further structural studies were performed to elucidate the detailed fragment-level binding mechanisms to CYP2C19. The high-resolution X-ray crystal structure of human CYP2C19 complexed with (2-methyl-1-ofuran-3-yl)(4-hydroxy-3,5-dimethylphenyl)-methanone (PDB ID: 4GQS; 2.87 Å resolution) was selected due to its well-defined distal haem cavity and substrate-recognition sites (SRS-1 to SRS-4).[93] The critical residues include Ser208 and His99 (SRS-1) and the hydrophobic residues Phe114, Ile297, and Leu366 (SRS-4).

https://doi.org/10.1021/acsomega.5c04809
ACS Omega 2025, 10, 55325−55353

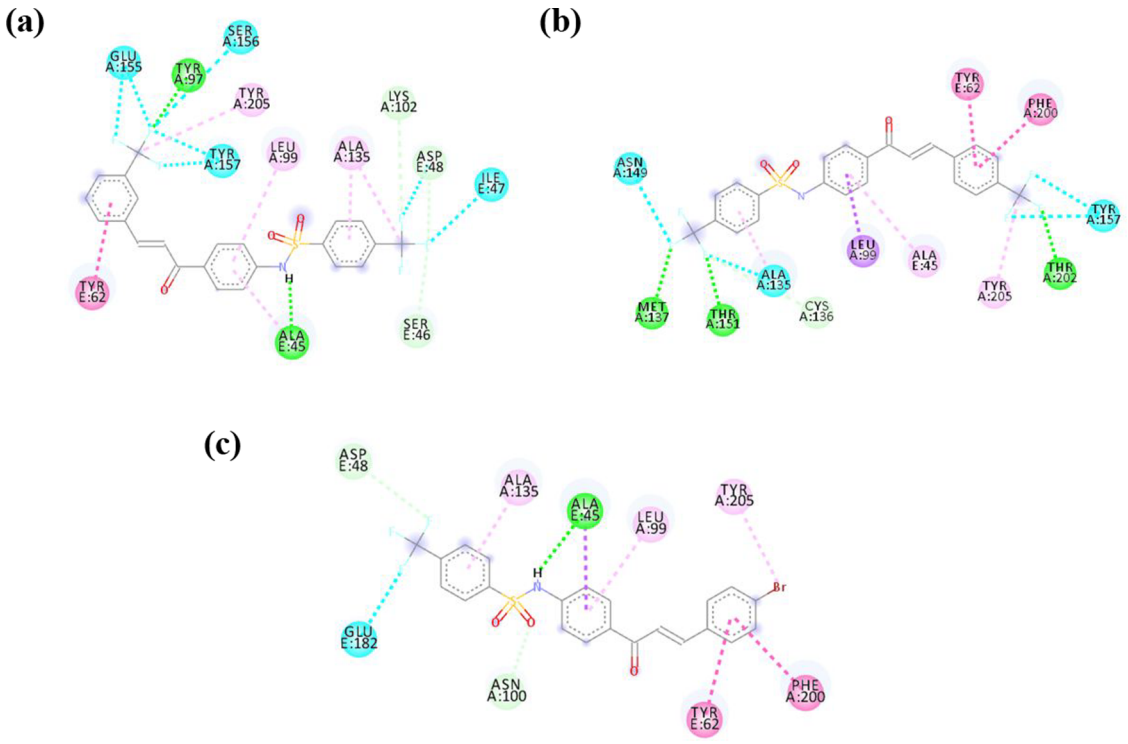

Figure 5. 2D representation of the binding interactions between the allosteric site of the $GABA_A$ receptor and the three highest scoring ligands, compounds (a) **19**, (b) **20**, and (c) **21**. Green line: H-bond; orange line: π−cation/anion; purple line: π−π-stack/T-form; light purple: alkyl/π-alkyl; cyan line: halogen (fluorine); yellow line: π-sulfur.

Table 6. Overall, Analysis of the Binding Interaction of Compounds 19, 20, and 21 with the Target $GABA_A$ Receptor[a]

		hydrogen bonds		halogens		π-cation/ π-sigma/π-stacking interactions		carbon H-bonds	
compound	target protein	amino acid	substituent	amino acid	substituent	amino acid	substituent	amino acid	substituent
19	4COF	Tyr97	−F	Glu155	−F	Tyr205	−F	Lys102	−F
		Ala45	N−H	Tyr157		Leu99	benzene	Asp48	
				Ile47		Ala135	−F	Ser46	
				Asp48		Tyr62	benzene		
20		Met137	−F	Asn149	−F	Leu99	benzene ring	Cys136	−F
		Thr151		Ala135		Tyr62			
		Thr202		Tyr157		Phe200			
21		Ala45	N−H	Glu182	−F	Tyr62	benzene ring	Asp48	−F
						Phe200		Asn100	S═O

[a]Abbreviations: MET, methionine; TYR, tyrosine; ALA, alanine; GLU, glutamic acid; GLY, glycine; ALA, alanine; LYS, lysine; ARG, arginine; THR, threonine; GLN, glutamine; ASP, aspartic acid; SER, serine; CYS, cysteine; ASN, asparagine; PHE, phenylalanine; LEU, leucine.

Table 7. Fragment Docking Energies, Ligand Efficiencies, and Key Interactions with CYP2C19 (PDB ID: 4GQS)

fragment/ compound	molecular formula	binding energy, ΔG (kcal/mol)	heavy atoms	ligand efficiency (LE) (kcal/mol)	key interactions
sulfonamide	$-SO_2NH-C-$	−3.374	6	0.56	H-bond (Ala297), π-sigma (HEM501)
trifluoromethyl	$-CF_3$	−3.448	4	0.86	halogen (HEM501), π-alkyl (Ile362, Leu366)
chalcone	−CO−CH═CH−	−3.143	4	0.79	H-bond (Ala297)
phenyl	C_6H_5	−4.422	6	0.74	π−π T-shaped and π-alkyl (HEM501)
fluorine	−F	−1.068	1	1.07	no interaction
chlorine	−Cl	−1.177	1	1.18	hydrophobic (Ile178, Ile181, Leu131 & Leu294)
bromine	−Br	−1.231	1	1.23	no interaction
compound **19**	$C_{23}H_{15}F_6NO_3S$	−6.493	34	0.19	hydrophobic (Ile205 & Glu300), H-Bond (Asn107)
compound **20**	$C_{23}H_{15}F_6NO_3S$	−4.622	34	0.19	H-bond (Asp293), halogen bond (Thr304 & Ser478), hydrophobic (Thr301)
compound **21**	$C_{22}H_{15}BrF_3NO_3S$	−8.408	31	0.27	halogen (Asn107 & Ile289), hydrophobic (Thr301 & Ile362)

https://doi.org/10.1021/acsomega.5c04809
ACS Omega 2025, 10, 55325−55353

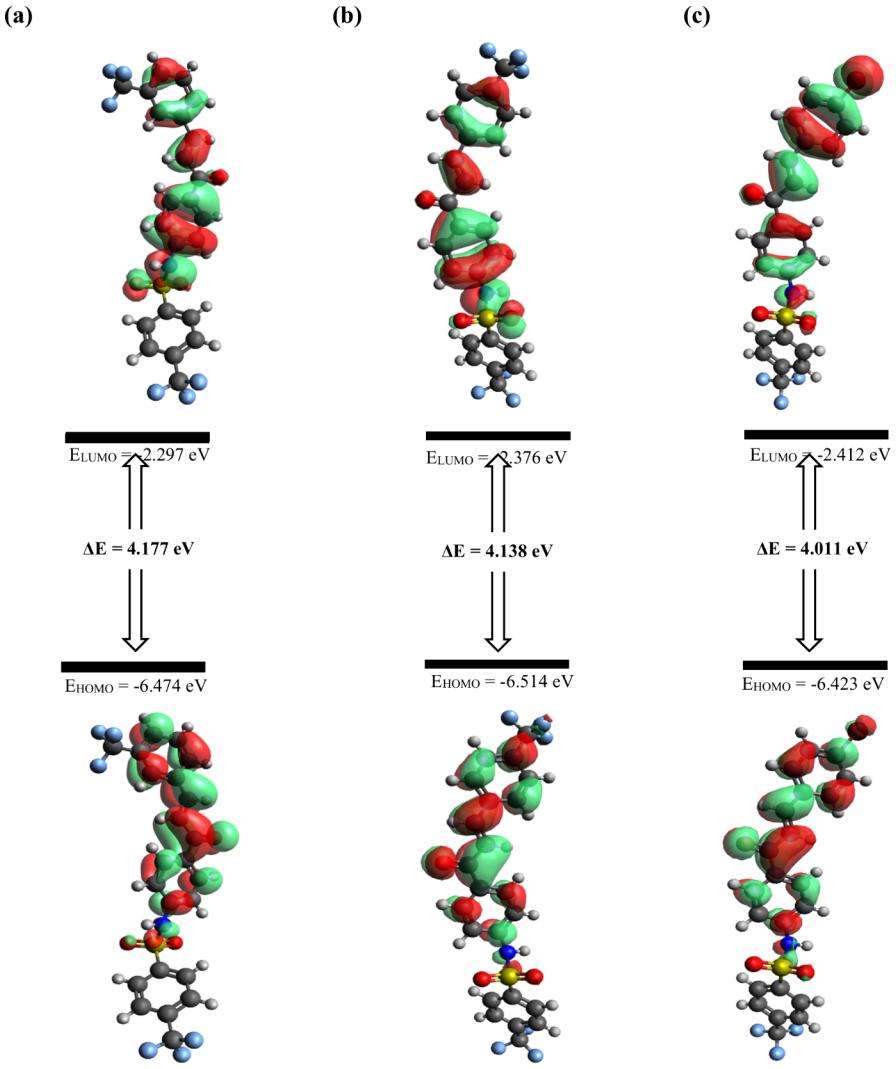

Figure 6. HOMO and LUMO molecular orbitals and their energy levels for compounds (a) **19**, (b) **20**, and (c) **21**, and were calculated using the DFT/B3LYP/def-SV(P) method.

Seven chemical molecular fragments (representing common drug substructures) were docked to CYP2C19, and their binding free energies (ΔG) and ligand efficiencies (LE) were calculated (Table 7). This fragment-based SAR analysis highlighted two key structural features required for CYP2C19 inhibition: a polar headgroup forming H-bonds with key residues Ser208 and His99 in SRS-1, and a hydrophobic or aromatic core interacting via $\pi-\pi$ and π-alkyl in SRS-4.[94,95]

The sulfonamide fragment ($-SO_2NH-$) demonstrated the importance of the polar headgroup, with moderate binding affinity (ΔG = −3.37 kcal/mol, LE = 0.56 kcal·mol^{-1}·HA^{-1}) through H-bonds with Ala297 and π−sigma contacts with the porphyrin edge, effectively anchoring it near the haem iron. Similarly, the chalcone carbonyl group ($-CO-CH=CH-$) formed H-bonds with Ala297 (ΔG = −3.14 kcal/mol, LE = 0.79 kcal·mol^{-1}·HA^{-1}), confirming its dual function as a H-bond acceptors and π-systems for anchoring in the active site. The phenyl ($-C_6H_5$) fragment showed the highest binding affinity (ΔG = −4.42 kcal/mol, LE = 0.74 kcal·mol^{-1}·HA^{-1}), forming $\pi-\pi$ T-shaped and π-alkyl interactions with the HEM501 (the haem group), emphasizing the crucial role of the aromatic nuclei in binding.

In contrast, the monohalogen fragments displayed varying interactions and affinities: Fluorine (−F) had minimal affinity (ΔG = −1.07 kcal/mol, LE = 1.07 kcal·mol^{-1}·HA^{-1}), chlorine (−Cl) interacted hydrophobically with Ile178, Ile181, Leu131, and Leu294 (ΔG = −1.18 kcal/mol, LE = 1.18 kcal·mol^{-1}·HA^{-1}) and bromine (−Br) had no specific interactions (ΔG = −1.23 kcal/mol, LE = 1.23 kcal·mol^{-1}·HA^{-1}). The trifluoromethyl group ($-CF_3$) bound moderately (ΔG = −3.45 kcal/mol, LE = 0.86 kcal·mol^{-1}·HA^{-1}), interacting via H-bonds with the haem and π-alkyl interactions with Ile362 and Leu366.

Translating the fragment-based findings to the full sulfonamide−chalcone structures, compound **19** showed a strong binding affinity (ΔG = −6.49 kcal/mol, LE = 0.19 kcal·mol^{-1}·HA^{-1}) through hydrophobic and H-bond interactions. Compound **20** exhibited a lower binding affinity (ΔG = −4.22 kcal/mol, LE = 0.19 kcal·mol^{-1}·HA^{-1}) due to a less favorable geometry. Compound **21** with 4-bromophenyl substituent, showed the highest binding affinity in the series (ΔG = −8.41 kcal/mol, LE = 0.27 kcal·mol^{-1}·HA^{-1}) due to halogen and hydrophobic interactions.

These comprehensive results indicate that for effective CYP2C19 inhibition, the sulfonamide headgroup must be retained for anchoring in SRS-1, while a moderately large

https://doi.org/10.1021/acsomega.5c04809
ACS Omega 2025, 10, 55325−55353

aromatic core is incorporated into SRS-4, which is optimized for $\pi-\pi$ and halogen interactions. While the superior binding affinity of compound **21** underscores the value of polarizable halogens-substituted aromatic cores, it was predicted that increased lipophilicity and excessive binding affinity present risks for prolonged enzyme occupancy and increased drug−drug interaction (DDI) liability. Compound **19** offers a balanced approach to potency and LE through its dual $-CF_3$ substituents, while compound **20** illustrates the critical sensitivity of core substitution patterns to binding geometry. These structure-based insights provide a clear framework for rational drug optimization: maintaining polar headgroups alongside Ser208 and His99, carefully tuning aromatic core substituents to optimize π and halogen-binding interactions in SRS-4 and avoiding overly lipophilic groups that could exacerbate CYP2C19 inhibition and increase the risk of metabolic DDIs.

3.4. Density Functional Theory (DFT) Analysis. DFT is a computational quantum mechanical method that provides insights into molecular stability and reactivity and complements molecular docking predictions for active structures **19**, **20**, and **21**. By analyzing the energies of the frontier molecular orbitals (FMOs), in particular the highest occupied molecular orbital (HOMO) and the lowest unoccupied molecular orbital (LUMO), DFT calculations provide valuable information on ionization potential (IP), electron affinity (EA), electronegativity (χ), electrophilicity index (ω), hardness (η), softness (s), and chemical potential (μ).[96−98] These parameters help to establish the relationship between energy, structure and reactivity, which is crucial for understanding the interaction of the predicted compounds with the $GABA_A$ receptor. The HOMO (E_{HOMO}), LUMO (E_{LUMO}) and gap energies (ΔE_{gap}) were determined using DFT/B3LYP/def-SV(P) in the gas phase, allowing the evaluation of molecular stability and electronic properties. The ΔE_{gap} values, indicative of chemical reactivity, corroborate the docking results by confirming that compounds **19**, **20**, and **21** possess favorable electronic configurations for strong receptor binding. This integrative approach strengthens the hypothesis that these compounds act as potent $GABA_A$ receptor antagonists and supports their potential as alternative drug candidates for epilepsy treatment.

3.4.1. Frontier Molecular Orbitals (FMOs) and Global Descriptor. FMOs, including the HOMO and the LUMO, are often used to study the chemical reactivity and regioselectivity.[99] The calculated HOMO and LUMO energies together with the corresponding ΔE_{gap} for compounds **19**, **20**, and **21** are presented in Figure 6. These three compounds belong to the same structural series, but differ in important substituent features: compounds **19** and **20** differ in the position of their substituents (*para* vs *meta*), while compound **21** bears a *para*-bromo instead of a trifluoromethyl ($-CF_3$) group. These structural variations directly influence their FMO energies and global reactivity descriptors. The calculated ΔE_{gap} for compounds **19**, **20**, and **21** are 4.177, 4.138, and 4.011 eV, respectively, using the B3LYP/def-SV(P) theory level. These values fall within the typical ΔE_{gap} region observed for many bioactive organic molecules. For example, a ΔE_{gap} of 4.02 eV was determined for flunitrazepam, a well-known BZD and $GABA_A$ receptor modulator, in a DFT study,[100] which closely matches the ΔE_{gap} of compound **21**. In addition, these values are significantly lower than those of benzene (∼6 eV), which emphasizes the increased reactivity and lower kinetic stability of the sulfonamide-chalcones studied, which could be advantageous for drug-receptor interactions.

Of the three compounds, compound **21** exhibits the highest electron-donating and electron-accepting capabilities, as evidenced by the highest HOMO energy (E_{HOMO} = −6.423 eV), the lowest ionization potential (IP = 6.423 eV), the lowest LUMO energy (−2.412 eV) and the highest electron affinity (EA = 2.412 eV). Since the ionization potential (IP) correlates directly with the HOMO energy, a higher (less negative) HOMO indicates a lower IP, which means that the molecule can donate electrons more easily, improving its nucleophilic behavior and overall reactivity toward electrophilic targets. Furthermore, compound **21** has the smallest ΔE_{gap} (4.011 eV) among the three compounds, indicating greater chemical reactivity, lower kinetic stability and higher polarizability. This increased polarizability can be attributed to the presence of bromine, which allows easier distortion of electron density under an electric field due to its larger atomic size and lower electronegativity compared to fluorine. The order of stability based on the ΔE_{gap} values is **19** > **20** > **21**, with corresponding ΔE_{gap} of 4.177, 4.138, and 4.011 eV (Figure 6). These trends are consistent with literature reports showing that CF_3-substituted aromatic compounds typically have ΔE_{gap} of ∼4.0−4.5 eV, while Br-substituted compounds have slightly lower gaps (∼3.8−4.2 eV). A smaller ΔE_{gap} is a hallmark of a "soft" molecule, more chemically reactive and more likely to undergo drug-receptor interactions.[101,102]

In contrast, compound **19** with the largest ΔE_{gap} behaves like a "hard" molecule, characterized by lower polarizability, higher kinetic stability and a lower tendency to deform the electron cloud. This makes it less reactive, as the absorption of electrons into a high-lying LUMO is less energetically favorable. To further explore their electronic properties, global reactivity descriptors, including ionization potential (IP), electron affinity (EA), electronegativity (χ), electrophilicity index (ω), hardness (η), softness (S) and chemical potential (μ), were calculated using Koopmans' theorem (Table 8).[103,104] The chemical potential (μ) reflects the tendency of the molecule to lose electrons. All three compounds have negative μ values (−4.386, −4.445, and −4.418 eV), indicating inherent stability and resistance to spontaneous degradation. The hardness (η) quantifies the resistance to electronic deformation and correlates with the ΔE_{gap}.[105] Compounds **19**, **20**, and **21** exhibit η-values of 2.089, 2.069, and 2.006 eV, respectively, confirming a decreasing trend in stability and an increasing trend in chemical reactivity throughout the series.

Table 8. Calculation of Global Reactivity Descriptors Using DFT/B3LYP/def-SV(P) Method in Gas State

compounds	19	20	21
E_{HOMO} (eV)	−6.474	−6.514	−6.423
E_{LUMO} (eV)	−2.297	−2.376	−2.412
$\lvert E_{HOMO} - E_{LUMO} \rvert$ (eV)	4.177	4.138	4.011
ionization potential (eV)	6.474	6.514	6.423
electron affinity (eV)	2.297	2.376	2.412
electronegativity, χ (eV)	4.386	4.445	4.418
chemical potential, μ (eV)	−4.386	−4.445	−4.418
global hardness, η (eV)	2.089	2.069	2.006
global softness, s (eV)	1.045	1.035	1.003
electrophilicity index, ω (eV)	4.604	4.775	4.865

https://doi.org/10.1021/acsomega.5c04809
ACS Omega 2025, 10, 55325−55353

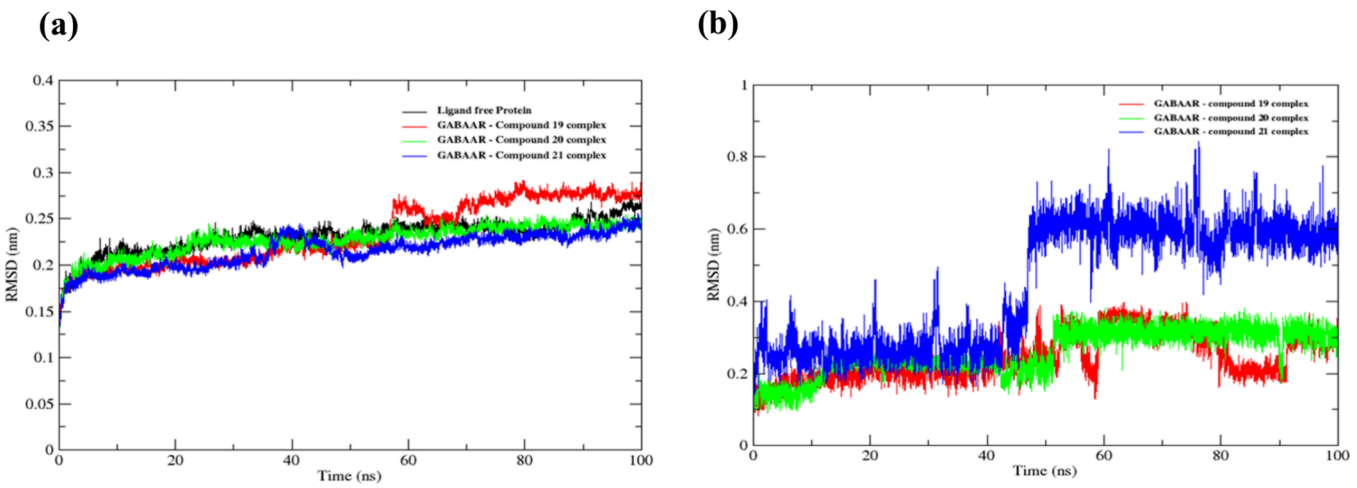

Figure 7. RMSD plot of (**a**) $GABA_AR$ protein backbone in complex with selected sulfonamide-containing chalcones and (**b**) selected sulfonamide-containing chalcones (compounds **19**, **20**, and **21**) backbone in complex with $GABA_AR$.

Softness (S), the reciprocal of hardness, and the electrophilicity index (ω) provide further insight into the reactivity profiles. Remarkably, compound **21** exhibits the highest electrophilicity (ω = 4.865 eV), indicating a strong tendency to accept electrons and associate with electron-rich biological targets. This increased reactivity suggests that compound **21** could effectively interact with nucleophilic sites such as DNA bases or protein thiol groups, which may contribute to both therapeutic activity and potential off-target toxicity. The molecular docking results indicate that compound **20** may have a better physical fit within the target binding site, while compound **21** is likely to form stronger electronic interactions due to its favorable reactivity descriptors. Therefore, both compounds were selected for further evaluation using advanced computational techniques, including molecular dynamics simulations, to further determine their potential as lead candidates.

3.4.2. Mulliken Population Analysis. Mulliken population analysis is one of the most widely used models for predicting individual atomic charges and remains computationally popular in calculations due to its simplicity. The atomic charges of selected compounds **19**, **20**, and **21** (Supplementary Figure S5) were calculated with Mulliken population analysis using the B3LYP method with def-SV(P) basis set,[106] as summarized in Supplementary Table S6. Mulliken charge analysis shows that all hydrogen atoms carry positive charges, with H-37, H-33, and H-33 having relatively high values of 0.090, 0.090, and 0.089, respectively. These increased positive charges indicate possible intra- and intermolecular hydrogen bonding within the crystal packing. Of all the compounds, H-11 has the highest positive Mulliken charge (0.183), as it is directly bonded to the electronegative nitrogen atom. Conversely, the oxygen and nitrogen atoms carry the most negative charges due to their high electronegativity. In addition, carbon atoms bonded to oxygen and nitrogen have positive charges, reflecting their electron-withdrawing nature. Overall, the Mulliken charge distribution illustrates the key electronic properties of these compounds, particularly the influence of the electronegative atoms on charge polarization and potential hydrogen bonding, which are crucial for their structural stability and reactivity.

3.4.3. Molecular Electrostatic Potential (MESP) Maps. Electrostatic potential (ESP) maps visually represent the charge distribution in a molecule and help to identify electrophilic and nucleophilic sites that are critical for the development of AEDs targeting the $GABA_A$ receptor. In the molecular ESP (MESP) of compounds **19**, **20**, and **21**, the most negative regions (red) are located around the oxygen atoms in the S═O and C═O groups, characterizing them as likely sites for electrophilic attack. Conversely, the nitrogen atoms appear in the most positive regions (blue), indicating potential sites for nucleophilic attack. Some negative potential is also distributed along the carbon−carbon double bonds of the ring. These charge patterns, shown in Supplementary Figure S6, provide insight into the local reactivity and interaction sites of the molecules.

These observations are consistent with the global reactivity parameters derived from DFT, which further characterize the overall chemical behavior of the compounds. Based on the DFT results, compound **21** emerges as the most chemically reactive, with the smallest ΔE_{gap}, the highest electrophilicity index (ω) and strong electron donating and accepting capabilities. These properties may increase its binding affinity to the $GABA_A$ receptor by facilitating favorable electrostatic and charge transfer interactions. However, the high reactivity and pronounced electrophilicity also raise concerns about potential off-target toxicity. Highly reactive compounds can interact nonspecifically with biological macromolecules such as proteins and enzymes or be metabolically activated to form toxic intermediates.[107,108] In particular, strong electrophiles can form covalent bonds with nucleophilic sites on DNA or proteins, which can lead to cell damage or immunogenic reactions. In contrast, compound **19** with the largest ΔE_{gap} is the most stable and least reactive compound, which could reduce its effectiveness as a $GABA_A$ receptor antagonist. Compound **20**, which has an intermediate ΔE_{gap} and ω value, provides a favorable balance between stability and reactivity. This balanced profile is supported by molecular docking results showing strong antagonistic interactions with the $GABA_A$ receptor. Therefore, compound **20** was selected for further evaluation through molecular dynamics (MD) simulations to assess its binding stability, conformational flexibility, solvation behavior and interaction dynamics in a biological environment, the key parameters for advancing the development of $GABA_A$-targeted therapies for epilepsy.

https://doi.org/10.1021/acsomega.5c04809
ACS Omega 2025, 10, 55325−55353

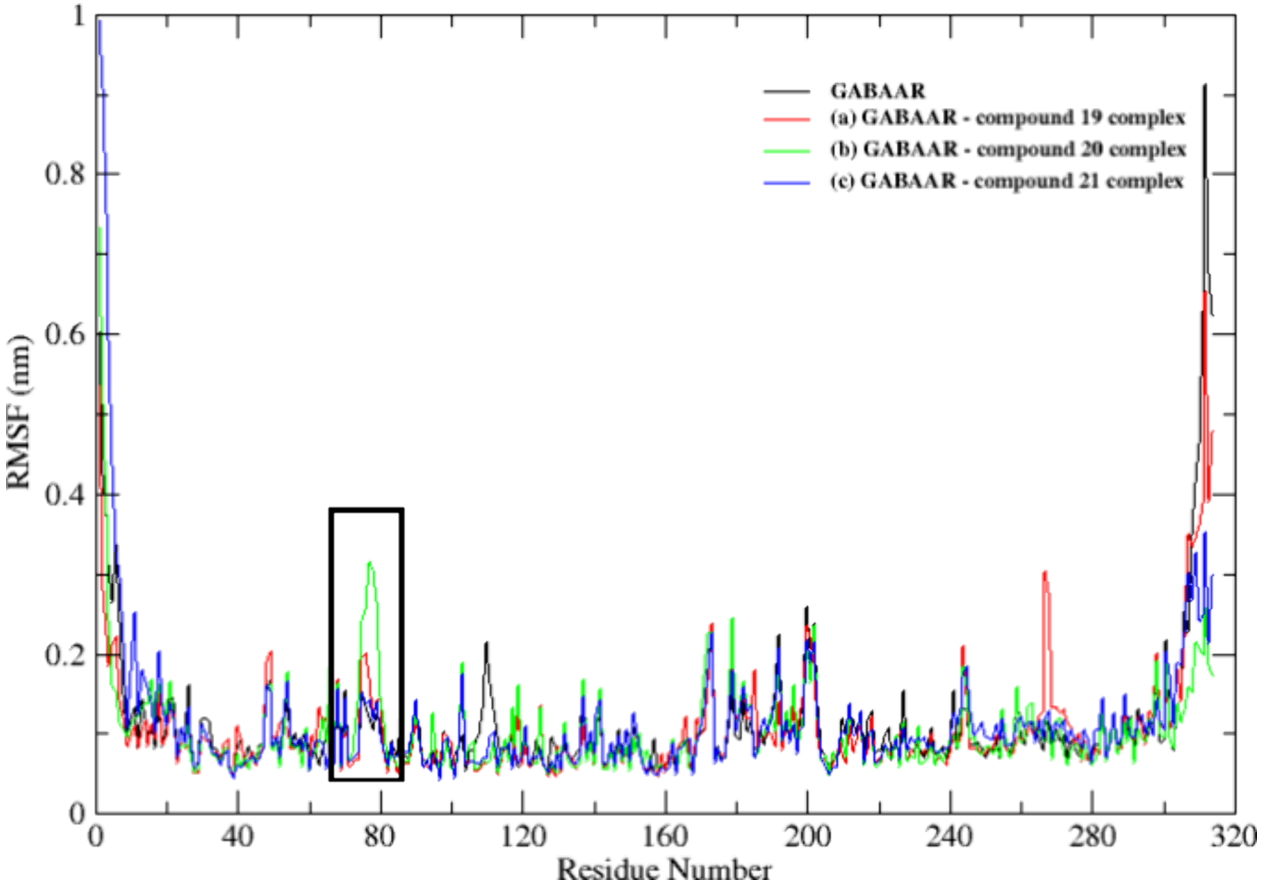

Figure 8. RMSF plot compares the behavior of all atoms in the $GABA_AR$ when it is bound or unbound to the respective compounds **19**, **20**, and **21**. The unbound $GABA_AR$ is shown in black in (a) $GABA_AR$-compound **19**, (b) $GABA_AR$−compound **20**, and (c) $GABA_AR$-compound **21**..

3.5. Molecular Dynamics Simulation. MD simulation is a computer-aided tool used in structure-based drug design to predict the protein−ligand stability and interactions in dynamic environment.[109,110] In this study, MD simulations were used in combination with a simulation interaction diagram (SID) to analyze deviations, fluctuations and intermolecular interactions.[111] A classical atomistic 100 ns SPC water model was used to investigate the docking dynamics of the three compounds (**19**, **20**, and **21**) with the highest binding affinity. Key parameters such as RMSD, RMSF, R_g, SASA, and H-bonds were evaluated to provide insights into the structural stability and binding mechanisms of protein−ligand complexes to support drug optimization strategies.

3.5.1. Root Mean Square Deviation (RMSD) and Root-Mean-Square Fluctuation (RMSF). The RMSD is a key metric in MD simulations to evaluate the stability of proteins and protein−ligand complexes over time.[112] In this study, the RMSD was used to evaluate the deviations in the $GABA_AR$ backbone, focusing on the stability of the $GABA_AR$-chalcone complexes during the 100 ns simulation. Lower RMSD values generally indicate greater stability. As shown in Figure 7a, the average RMSD values for $GABA_AR$-compound **19**, $GABA_AR$-compound **20**, and $GABA_AR$-compound **21** were 0.26, 0.22, and 0.20 nm, respectively. Initially, the RMSD varied between 0.18−0.27 nm for compound **19**, 0.16−0.24 nm for compound **20** and 0.11−0.24 nm for compound **21**. The RMSD diagram shows that the complex of $GABA_AR$-compound **20** exhibited the highest stability as its structure deviated the least compared to compounds **19** and **21**. Figure 7a also shows that all sulfonamide-chalcone-bound complexes exhibited RMSD deviations in the first 20 ns, followed by minimal fluctuations between 30 and 60 ns. At the end of the simulation, the minimum RMSD values were 0.280, 0.250, and 0.241 nm for compounds **19**, **20**, and **21**, respectively. Remarkably, compounds **20** and **21** had lower RMSD values than the unbound $GABA_AR$ (0.267 nm). The RMSD of the complex of $GABA_AR$-compound **20** stabilized after 23 ns and kept the fluctuations low, indicating a stable binding interaction. Throughout the MD simulation, compounds **20** and **21** showed the smallest deviations, indicating strong and stable interactions with $GABA_AR$. Contradictorily, compound **19** showed greater variation with RMSD values between 0.22 and 0.73 nm (average 0.45 nm), particularly between 40 and 50 ns (Figure 7b), suggesting weaker and less stable binding. Of all, compound **20** deviated the least from its original configuration, confirming its stability.

To evaluate the flexibility of the protein after ligand binding, the RMSF diagram (Figure 8) was analyzed. The variations were similar for all compounds, with significant deviations highlighted in the black box (Figure 8). The $GABA_AR$-compound **19** complex showed fluctuations in residues 265−280, while compound **20** showed fluctuations in residues 70−80. These fluctuations may reflect conformational changes or dynamic behavior. Overall, all $GABA_AR$-chalcone complexes exhibited greater fluctuations than unbound $GABA_AR$, likely due to ligand binding affecting protein dynamics.[113] Protein fluctuations during MD simulations indicate conformational

https://doi.org/10.1021/acsomega.5c04809
ACS Omega 2025, 10, 55325−55353

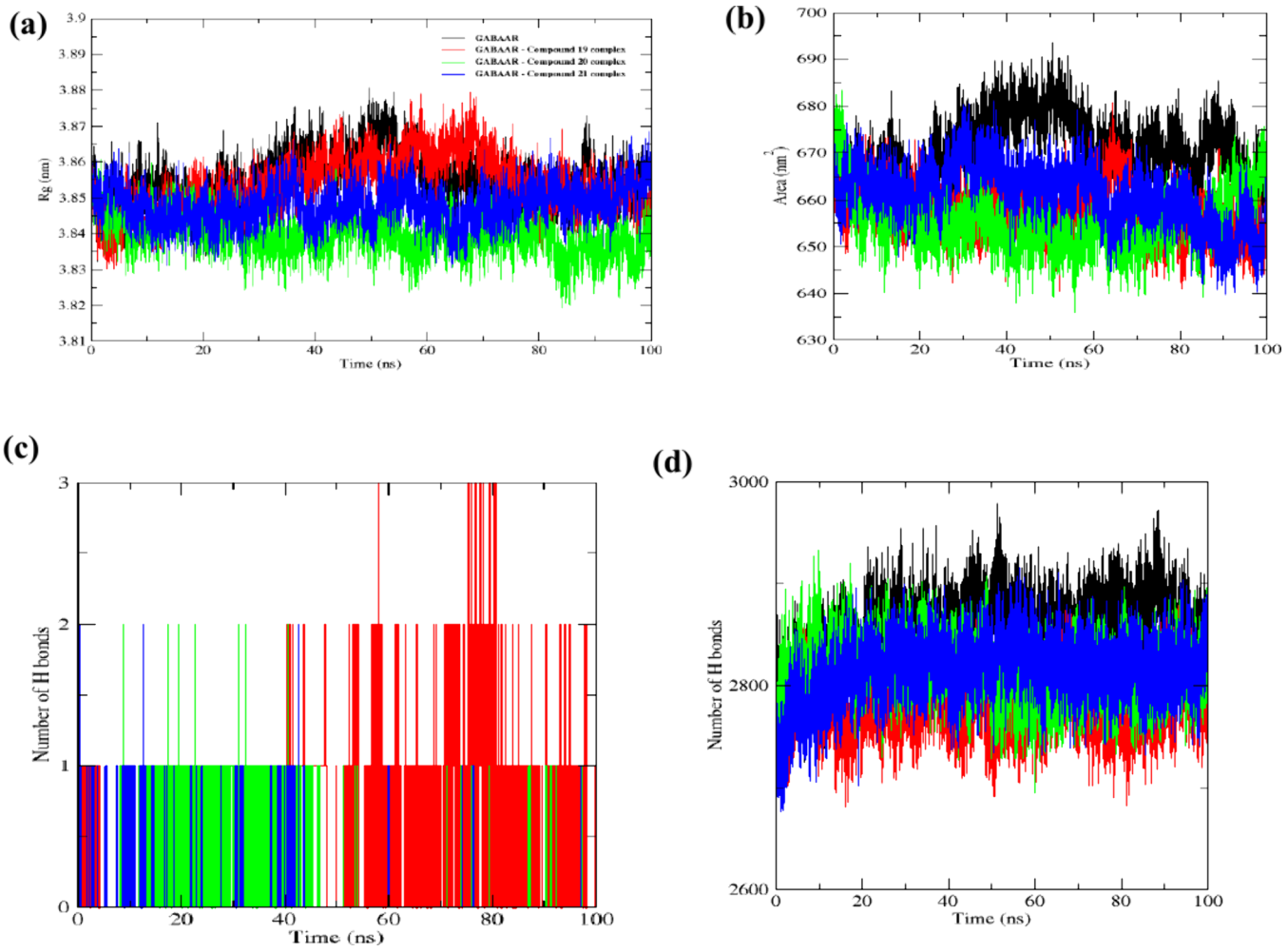

Figure 9. (a) The radius of gyrations (R_g) of the complexes, (b) solvent-accessible surface area (SASA) of the complexes, (c) number of H-bonds observed between $GABA_AR$ and the ligand, and (d) number of H-bonds between $GABA_AR$ and water molecules during MD simulation. Black: $GABA_AR$; red: $GABA_AR$-compound **19**; green: $GABA_AR$-compound **20**; blue: $GABA_AR$-compound **21**.

flexibility or structural changes in the protein−ligand complex over time.

3.5.2. Radius of Gyration (R_g), Solvent-Accessible Surface Area (SASA), and H-Bond Analyses. The Rg value measures the compactness of proteins by reflecting the mass distribution around an axis.[114] In protein−ligand interactions, R_g provides insights into conformational changes and the folding of the protein after ligand binding.[115] During the 100 ns MD simulation, unbound $GABA_AR$ maintained a stable R_g of 3.81 nm, indicating structural integrity. When bound to sulfonamide-chalcones (compounds **19**, **20**, and **21**), the average R_g values were 3.86, 3.84, and 3.85 nm, respectively (Figure 9a). These values suggest minimal conformational changes of the protein upon ligand binding. The fluctuations in R_g remained within 3.80−3.86 nm, indicating that all three ligands preserve the structural integrity of $GABA_AR$ while causing a slight increase in compactness. SASA was also analyzed to assess the exposure of the protein surface to solvent molecules, which affects ligand binding, protein−protein interactions and conformational changes.[116] Monitoring SASA during MD simulations helps to identify key residues involved in ligand binding and protein stability.[117] The average SASA values for the $GABA_AR$-ligand complexes were 665.20 nm^2 (compound **19**), 661.32 nm^2 (compound **20**), and 668.13 nm^2 (compound **21**) (Figure 9b). In particular, the lower SASA value for compound **20** indicates a more stable interaction with $GABA_AR$ compared to compounds **19** and **21**. Furthermore, H-bonds play a crucial role in the stabilization of biological molecules. The total number of H-bonds formed during the MD simulations is shown in Figure 9c. Compounds **20** and **21** formed two H-bonds with the active site pocket of $GABA_AR$, with compound **20** showing a higher frequency of maintaining these interactions than compound **21**. In contrast, compound **19** formed a maximum of three H-bonds but showed fewer interactions with the solvent environment. The binding stability of the $GABA_AR$ compound complexes was further investigated using 100 ns simulations in a solvent environment. Among the three compounds, $GABA_AR$-compound **20** showed the strongest H-bond interactions, while $GABA_AR$-compound **19** and $GABA_AR$-compound **21** showed fewer interactions with the solvent (Figure 9d).

Although classical positive allosteric modulators (PAMs) generally bind to well-characterized nonorthosteric sites, such as the BZD binding site, there is evidence that structurally diverse scaffolds, including chalconoids, can potentiate GABAergic signaling through interactions proximal to the orthosteric site. Among these, compound **20** exhibited high affinity and stable pocket occupancy, as evidenced by persistent

https://doi.org/10.1021/acsomega.5c04809
ACS Omega 2025, 10, 55325−55353

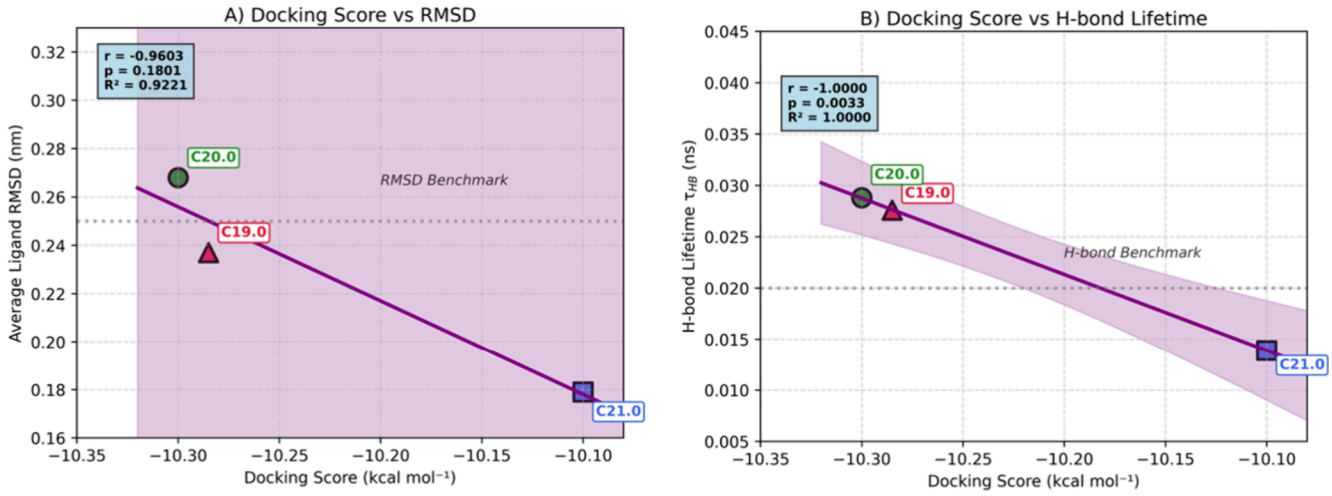

Compound	Dock Score	Avg RMSD	τ_{HB} (ns)
19	-10.3	0.237	0.0276
20	-10.3	0.268	0.0288
21	-10.1	0.179	0.0139

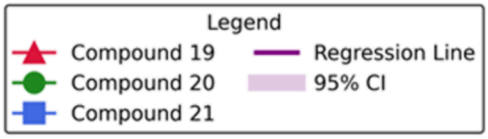

Figure 10. Correlation of docking scores with MD stability metrics for the potential hit AED candidates. (A) Inverse relationship between docking score and average ligand RMSD ($r = -0.960$, $p = 0.018$). (B) Direct relationship between docking score and H-bond lifetime (τ_{HB} ; $r = -1.000$, $p = 0.003$). Compound **20** (green) has a moderate RMSD and the longest τ_{HB}. The regression lines include 95% confidence intervals (CI), while the dashed reference values denote the stability thresholds in the literature.

H-bonding with key residues Thr151 and Thr202 and consistently low RMSD values during MD simulations. These results support that compound **20** acts as a nonclassical PAM by stabilizing the conformation of the $GABA_A$ receptor near the orthosteric site.

Collectively, the integrated findings from molecular docking, DFT and MD simulations indicate that compound **20** exhibits strong binding affinity, optimal electronic properties and high structural stability within the $GABA_AR$ binding site. Its favorable R_g, SASA and H-bond interactions support its stability and potential as a promising $GABA_AR$ antagonist. These results highlight compound **20** as a strong drug candidate for the treatment of epilepsy that warrants further experimental validation.

3.5.3. Quantitative Correlation of Docking Affinities with MD Stability Metrics. Following MD simulations, a quantitative correlation analysis was conducted to validate static docking predictions with the dynamic binding behavior. This analysis revealed that H-bond lifetime (τ_{HB}) was a statistically significant predictor of ligand stability, supporting the selection of compound **20** as a promising AED candidate. Although compounds **20** and **19** had an identical binding affinity of −10.3 kcal/mol, initial docking analysis indicated that compound **20** was more strongly associated with key residues of $GABA_A$ receptor, forming four H-bonds (Tyr97, Thr142, Tyr205, and Thr206), and a key salt bridge with Arg144. In contrast, compound **19** formed only three H-bonds and lacked the critical salt bridge. Subsequent 100 ns MD simulations confirmed the functional significance of these interactions and revealed a perfect and statistically significant correlation between docking scores and H-bond lifetimes ($r = -1.0000$, $p = 0.0033$; Figure 10b). Compound **20** exhibited a higher τ_{HB} (0.0288 ns) than compound **19** (0.0276 ns), which can be attributed to a higher ligand stability due to its broader interaction profile. Conversely, ligand RMSD did not correlate significantly ($p = 0.1801$; Figure 10a), suggesting that H-bond persistence is a more reliable indicator of stabilizing interactions than overall positional fluctuation for these high-affinity ligands. Compound **21**, which exhibited the slightly lower docking score (−10.1 kcal/mol), displayed the shortest τ_{HB} (0.0139 ns), further confirming this stability trend. These results confirm the predictive power of docking values for dynamic stability, especially for τ_{HB}, and emphasize the robustness of compound **20** as a hit candidate for AED.

3.6. Synthesis and Characterization of Sulfonamide-Chalcones. All three target sulfonamide−chalcones (compounds **19**, **20**, and **21**) were successfully synthesized via a two-step route, sulfonylation of 4-aminoacetophenone, followed by a Claisen−Schmidt condensation with appropriately substituted benzaldehydes. In the ^{1}H NMR spectra, each compound exhibited diagnostic *trans*-alkene doublets ($J \approx 15.6$ Hz), confirming the exclusive formation of the *E*-isomer. The aromatic proton signals confirmed the expected substitution pattern, with pronounced deshielding (δ 8.02−8.06 ppm) for protons in *ortho* position to electron-withdrawing sulfonyl and carbonyl groups. Compounds with $-CF_3$ substituents showed atypically strong *meta*-couplings (~8−9 Hz), in line with the polar field effects reported for trifluoromethylbenzenes. In ^{13}C NMR, the α,β-unsaturated carbonyl carbons resonated at δ 189−197 ppm, which is characteristic of conjugated ketones. DI-MS analysis confirmed the molecular ions at m/z 499.0 [M]+ (for compounds 19 and 20) and 511.0 [M]+ (compound 21), with no evidence of fragmentation, validating the molecular integrity of the sulfonamide−chalcone scaffold. Meanwhile, the FTIR spectra displayed characteristic bands for N−H (3200−3300 cm^{-1}), C═O (1650−1680 cm^{-1}), and

https://doi.org/10.1021/acsomega.5c04809
ACS Omega 2025, 10, 55325−55353

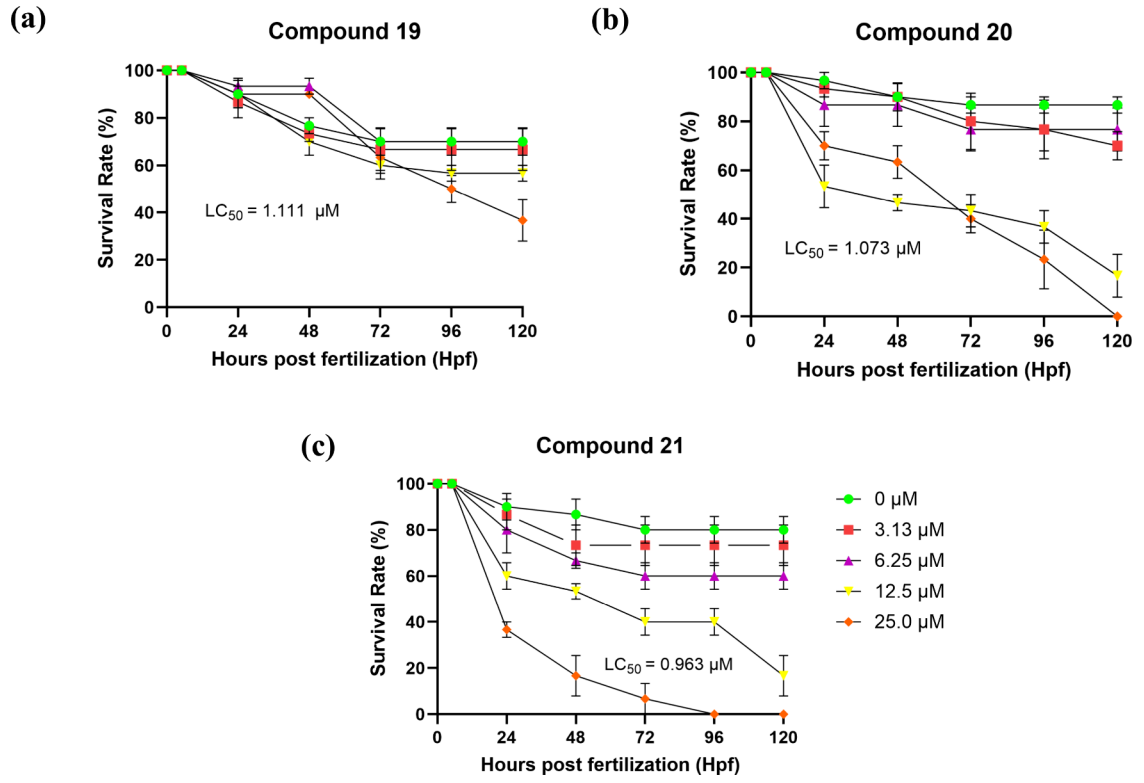

Figure 11. Survival rate of zebrafish embryos over 120 hpf when exposed to compounds (a) **19**, (b) **20**, and (c) **21**. Results are presented as mean ± SEM (n = 10).

aromatic/alkenic C−H stretches, further confirming the presence of the main functional groups of the targeted compounds. The observed melting points and R_f values were in agreement with structurally related analogues, indicating high purity and successful purification. Collectively, these findings affirm the efficient synthesis of the sulfonamide-chalcones and highlight the consistent electronic influence of the dual electron-withdrawing substituents on their spectroscopic profiles.

3.7. Preliminary Mortality Evaluation. To complement the computational results (Sections 3.1−3.4), a preliminary evaluation of the toxicity of the synthesized compounds **19**, **20**, and **21** was performed in order to gain an early insight into their safety profiles prior to the antiepileptic evaluation. This assessment, expressed as a median lethal concentration (LC_{50}), provides an initial indication of the relative toxicity of individual compounds. As shown in Figure 11, compound **19** had the highest LC_{50} value (1.11 μM), followed by compounds **20** (1.07 μM) and 21 (0.96 μM), indicating that compound **19** is the least toxic and compound **21** is the most acutely toxic. These mortality results provide an important experimental perspective in addition to the in silico predictions. Of note, DFT analysis identified compound **21** as the most chemically reactive, with the smallest ΔE_{gap} (4.011 eV), while compound **19** was the most electronically stable (ΔE_{gap} = 4.177 eV) and compound **20** was in between (ΔE_{gap} = 4.138 eV). The trend in toxicity (**21** > **20** > **19**) mirrors the trend in chemical reactivity and indicates a possible correlation between higher electronic reactivity and increased acute toxicity. This correlation suggests that the high reactivity of compound **21**, while potentially increasing binding to the target, may also lead to greater off-target interactions or metabolic instability, contributing to its observed toxicity. In contrast, the lower reactivity and greater stability of compound **19** are consistent with its lower toxicity, but may limit its pharmacodynamic efficacy. Compound **20** with moderate reactivity and toxicity has a balanced profile. It shows strong binding affinity, acceptable dynamic stability and tolerable toxicity. Overall, the preliminary toxicity data not only validate and refine the computational predictions, but also help to prioritize candidates for further in vivo efficacy studies. Compound **20** emerges as the most promising candidate as it shows a good balance between reactivity, safety and predicted pharmacological performance.

3.8. Preliminary Anti-Epileptic Behavioral Studies. To further validate their antiepileptic effects, compounds **19**, **20**, and **21** were tested with the chemoconvulsant PTZ-induced zebrafish larvae, an established model for seizure-like behavior caused by $GABA_A$ receptor antagonism and neuronal hyperexcitation.[118] The effects of these compounds were assessed by analyzing locomotor activity, a reliable marker of neuronal function and neurotoxicity. PTZ exposure typically induces pronounced seizure-like behaviors in zebrafish, including hyperactivity, rapid circling, clonus-like convulsions, and postural damage.[119−121] This model was selected due to its widely accepted as an effective in vivo platform for screening anticonvulsant candidates due to its reproducibility and relevance to human epilepsy.[122,123]

In this study, 7 dpf zebrafish larvae were exposed to 2.5 mM PTZ, a concentration optimized to induce strong seizures without causing death. Exposure of zebrafish larvae at 7 dpf for locomotor assessment in epilepsy studies since 7 dpf zebrafish larvae have a fully developed CNS and show coordinated swimming behavior, besides their BBB is functionally established. VPA (100 μM) was used as a positive control, with both concentrations selected based on previous studies

https://doi.org/10.1021/acsomega.5c04809
ACS Omega 2025, 10, 55325−55353

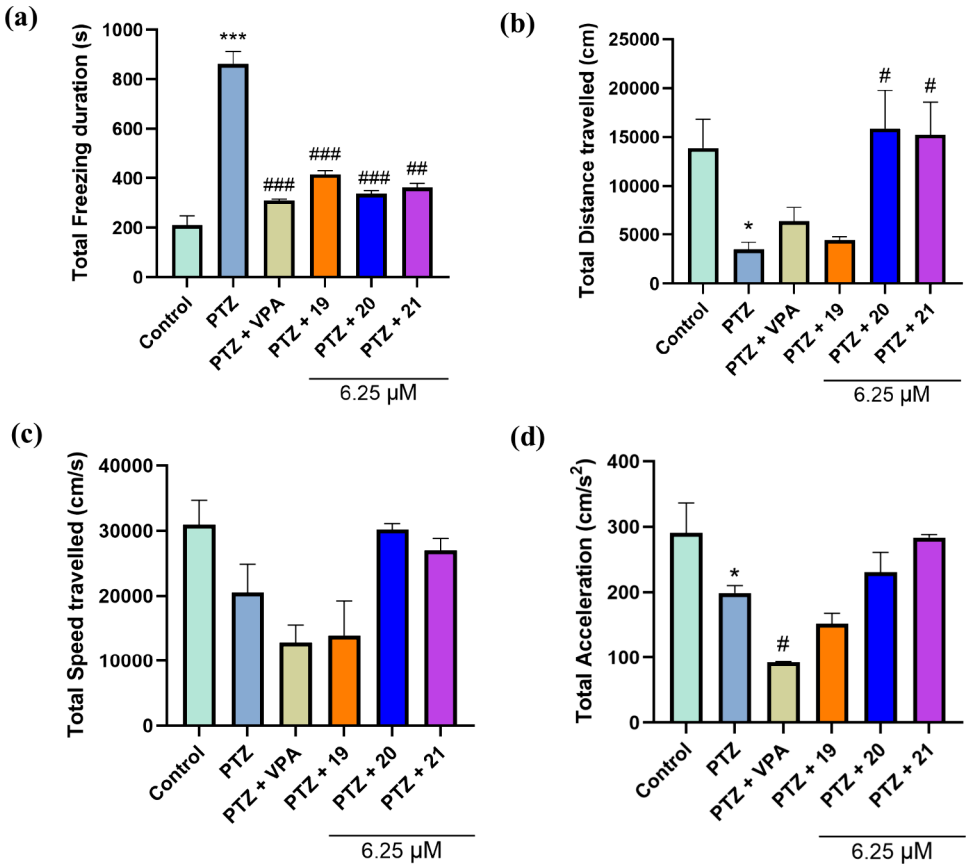

Figure 12. Locomotor activity in PTZ-induced larvae of zebrafish exposed to the tested compounds at 7 dpf (days postfertilization) at a concentration of 6.25 μM. (a) Total freezing count, (b) total distance traveled, (c) total speed traveled, and (d) total acceleration. Results are presented as mean ± SEM (n = 6). Statistical analysis was performed using a one-way ANOVA test followed by Tukey post-test; compared to control (*p < 0.05, **p < 0.01, ***p < 0.001) and compared to PTZ (#p < 0.05, ##p < 0.01, ###p < 0.001).

confirming safety. Seizure activity was assessed by analyzing locomotor behavior, which is a reliable indicator of neuronal function and neurotoxicity. Key parameters measured included total distance traveled, total speed and freezing behavior, an indicator of seizure severity, particularly in stage III seizures characterized by rigidity and sinking to the bottom of the tank.

The prolonged immobility observed in this study is more consistent with a stage III tonic−clonic seizure than an absence of ictal events.[47] By exposing zebrafish larvae to 2.5 mM PTZ for 10 min, followed by a 1-h treatment and acclimatization period prior to locomotor assessment, allows the capture of the full biphasic response [an initial hyperactivity phase (stage I−II)] immediately following PTZ exposure, transitioning to the later tonic−clonic/postictal phase with persistent freezing (stage III).[124] This delayed assessment differs from shorter (5−10 min) protocols that record behavior immediately after PTZ exposure, and therefore focuses primarily on hyperactivity,[125] leading to a more comprehensive evaluation of seizure severity, and thus improving sensitivity for acute and postictal anticonvulsant effects.

Compounds **19**, **20** and **21** were tested at two concentrations (6.25 and 3.13 μM; Figures 12 and 13), and behavior was assessed after 1 h of exposure. Zebrafish treated with PTZ alone showed significantly prolonged freezing time (immobility) compared to untreated controls (Figure 12a), indicating severe seizure activity. In contrast, treatment with VPA and all three sulfonamide-chalcones (compounds **19**, **20**, and **21**) significantly reduced the freezing time and improved the total distance traveled (Figure 12b), total speed (Figure 12c) and total acceleration (Figure 12d), indicating a protective effect against PTZ-induced seizures.

At 6.25 μM, all compounds resulted in more pronounced behavioral improvements compared to 3.13 μM, indicating dose-dependent antiepileptic activity (Figure 13). Although all three compounds attenuated seizure-like behaviors, compounds **20** and **21** showed greater efficacy than compound **19**, as evidenced by a greater increase in total distance traveled and reduced immobility. However, efficacy must be interpreted in the context of toxicity profiles. Compound **21** showed a strong recovery in behavior but also exhibited higher acute toxicity, limiting its suitability for further development. Conversely, compound **20** showed comparable anticonvulsant efficacy with significantly lower toxicity, highlighting its favorable safety/efficacy balance. In summary, compounds **19**, **20**, and **21** effectively attenuated PTZ-induced epileptic behavior in zebrafish larvae by restoring normal locomotor activity. Among them, compound **20** proved to be the most promising candidate for further investigation as it exhibits strong antiepileptic potential with a more favorable toxicity profile.

4. CONCLUSIONS

In summary, this study presents a series of newly designed aminated and sulfonamide-chalcones (compounds **1**−**36**) as potential $GABA_A$ receptor antagonists in the search for new AEDs. Molecular docking and MD simulations were

https://doi.org/10.1021/acsomega.5c04809
ACS Omega 2025, 10, 55325−55353

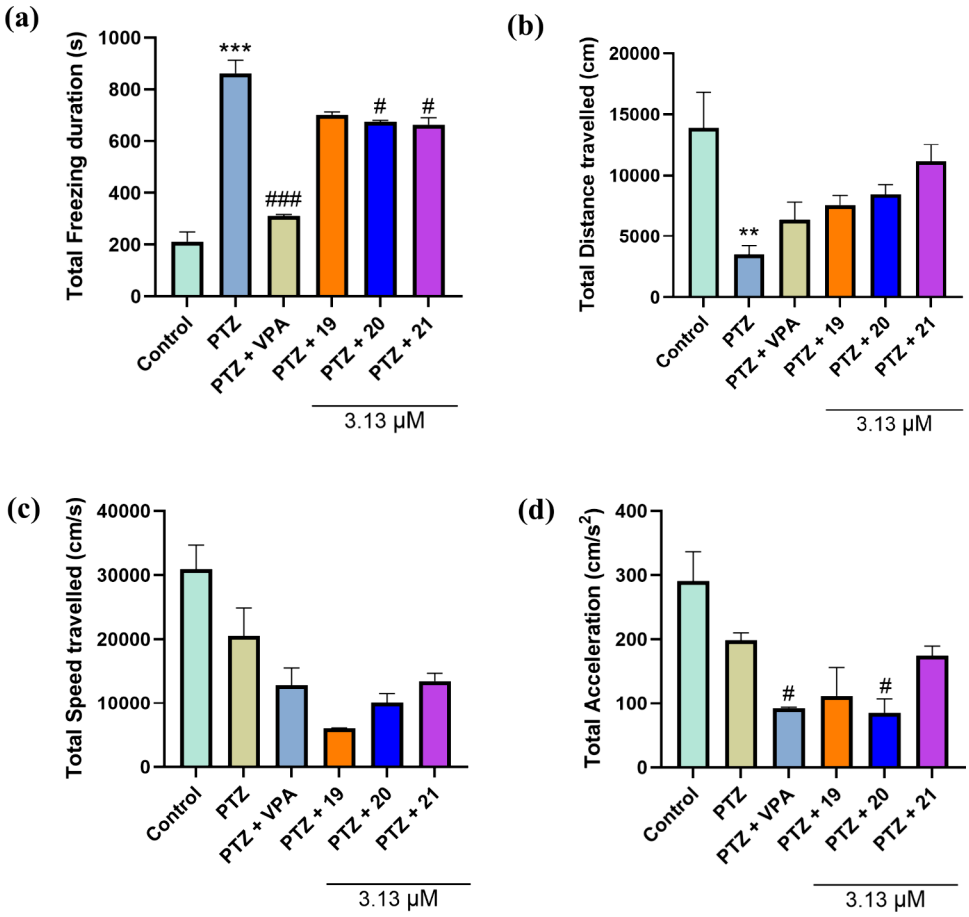

Figure 13. Locomotor activity in PTZ-induced larvae of zebrafish exposed to the tested compounds at 7 dpf (days postfertilization) at a concentration of 3.13 μM. (a) Total freezing count, (b) total distance traveled, (c) total speed traveled, and (d) total acceleration. Results are presented as mean ± SEM (n = 6). Statistical analysis was performed using a one-way ANOVA test followed by a Tukey post-test; compared to control (*p < 0.05, **p < 0.01, ***p < 0.001) and compared to PTZ (#p < 0.05, ##p < 0.01, ###p < 0.001).

performed to investigate their binding modes and complex stability with the target protein $GABA_AR$. The results showed high binding affinity and stable interactions, particularly for compounds **19**, **20**, and **21**, among which compound **20** was predicted to be the most promising candidate, supported by favorable drug-like properties, molecular docking results and MD stability parameters. MD simulation also showed that the $GABA_AR$ complexes with compounds **19**, **20**, and **21** exhibited higher stability compared to the unbound $GABA_AR$. Notably, the sulfonamide functionality was associated with the improved binding to the allosteric site and increased stability of the complex. To further corroborate the docking predictions, a quantitative correlation was performed between the docking results and the MD-derived parameters, particularly hydrogen bond lifetime (τ_{HB}) and ligand RMSD. The results showed a statistically significant correlation between docking affinity and τ_{HB} ($r = -1.0000$, $p = 0.0033$), confirming that compound **20** not only binds strongly but also forms persistent H-bonds, contributing to its superior complex stability. The antiepileptic potential of these compounds was then validated in vivo using the PTZ-induced epileptic zebrafish larvae. Behavioral assessment showed that compounds **19**–**21** significantly reduced PTZ-induced freezing behavior (stage III seizures) and improved key parameters of locomotion, including total distance traveled, speed, and acceleration. Taken together, these results suggest that compound **20** is a particularly promising AED candidate, with significant antiepileptic efficacy and a favorable toxicity profile. This compound warrants further investigation to be developed as safer and more effective chemotherapies for epilepsy. While the focus of this work is on advancing neurotherapeutics for human epilepsy, future work should also evaluate the environmental safety of such compounds through targeted ecotoxicological studies to assess potential agricultural and environmental impacts. This dual consideration will help ensure that both clinical efficacy and environmental safety are considered in the development of next generation AEDs.

■ ASSOCIATED CONTENT

Data Availability Statement

Data is provided within the article.

Supporting Information

The Supporting Information is available free of charge at https://pubs.acs.org/doi/10.1021/acsomega.5c04809.

Additional data for physicochemical, ADME, and toxicity predictions; detailed molecular docking validation and in-depth binding interaction analyses with 3D diagrams for all complexes; DFT calculations and molecular electrostatic potential maps; and ^{1}H NMR, ^{13}C NMR, FTIR, and DI-MS spectra for all synthesized compounds (PDF)

https://doi.org/10.1021/acsomega.5c04809
ACS Omega 2025, 10, 55325−55353

AUTHOR INFORMATION

Corresponding Author

Siti Munirah Mohd Faudzi − *Department of Chemistry, Faculty of Science and Natural Medicines and Product Research Laboratory, Institute of Bioscience, Universiti Putra Malaysia, Serdang, Selangor 43400, Malaysia;* orcid.org/0000-0001-8043-798X; Email: sitimunirah@upm.edu.my

Authors

Anis Nasuha Adzahar − *Department of Chemistry, Faculty of Science, Universiti Putra Malaysia, Serdang, Selangor 43400, Malaysia*

Nik Nur Farhana Nik Aizan − *Department of Chemistry, Faculty of Science, Universiti Putra Malaysia, Serdang, Selangor 43400, Malaysia*

Muhammad Alif Mohammad Latif − *Department of Chemistry, Centre of Foundation Studies for Agricultural Science, Universiti Putra Malaysia, Serdang, Selangor 43400, Malaysia;* orcid.org/0000-0002-3345-0265

Muhammad Syafiq Akmal Mohd Fahmi − *Natural Medicines and Product Research Laboratory, Institute of Bioscience, Universiti Putra Malaysia, Serdang, Selangor 43400, Malaysia*

Ahmad Zaidi Ismail − *Department of Chemistry, Faculty of Science, Universiti Putra Malaysia, Serdang, Selangor 43400, Malaysia*

Complete contact information is available at: https://pubs.acs.org/10.1021/acsomega.5c04809

Author Contributions

S.M.M.F. conceptualized the study, designed the methodology, managed the project and reviewed the final manuscript. A.N.A. performed the in silico prediction, docking, DFT and MD simulations, zebrafish antiepileptic studies and drafted the manuscript. M.A.M.L. supervised the MD simulation procedure and the platform. M.S.A.M.F. and N.N.F.N.A. provided guidance on zebrafish toxicity and antiepileptic studies. A.Z.I. supervised the DFT studies and workflow. All authors approved the manuscript.

Funding

This work was supported by the Universiti Putra Malaysia under Geran Putra Berimpak (GP-GPB/2022/9733100).

Notes

The authors declare no competing financial interest.

ACKNOWLEDGMENTS

This research was partially funded by Universiti Putra Malaysia under Geran Putra Berimpak (GP-GPB/2022/9733100), which provided necessary monthly assistance to the first author.

ABBREVIATIONS

ADMET, Adsorption, distribution, metabolism, excretion, toxicity; AED, Antiepileptic drug; BBB, Blood−brain barrier; BZD, Benzodiazepine; CNS, Central nervous system; DALYs, Disability-adjusted life years; GABA, γ-Aminobutyric acid; $GABA_A$, γ-Aminobutyric acid type-A; HB, Hydrogen bonding; HIA, Human intestinal absorption; MD, Molecular dynamics; NCDs, Noncommunicable diseases; PDB, Protein data bank; PPB, Plasma protein binding; Rg, Radius of gyration; RMSD, Root mean square deviation; RMSF, Root mean square fluctuation; SASA, Solvent accessible surface area; SBDD, Structure-based drug design; TPSA, Topological polar surface area; VPA, Valproic acid

REFERENCES

(1) Huang, Y.; Li, Y.; Pan, H.; Han, L. Global, Regional, and National Burden of Neurological Disorders in 204 Countries and Territories Worldwide. *J. Glob Health* **2023**, *13*, 4160.

(2) Stafstrom, C. E.; Carmant, L. Seizures and Epilepsy: An Overview for Neuroscientists. *Cold Spring Harb Perspect Biol.* **2015**, *7* (5), 1−19.

(3) Novak, A.; Vizjak, K.; Rakusa, M. Cognitive Impairment in People with Epilepsy. *J. Clin. Med.* **2022**, *11*, 267.

(4) Bilal, A.; Ullah, M. K.; Fatima, A.; Iqbal, K.; Kaleem Ullah, M.; Saleem Khan, M.; Nawaz, K.; Ali, U.; Qamer, S. A.; Sarfarz, A.; Nazar, I. Epilepsy: A Systematic Review JOJ Pub Health Epilepsy: A Systematic Review. *JOJ. Pub Health* **2021**, *6* (1), No. 555684.

(5) Anwar, H.; Khan, Q. U.; Nadeem, N.; Pervaiz, I.; Ali, M.; Cheema, F. F. Epileptic Seizures. *Discoveries* **2020**, *8* (2), No. e128.

(6) Jha, M.; Alam, O.; Naim, M. J.; Sharma, V.; Bhatia, P.; Sheikh, A. A.; Nawaz, F.; Alam, P.; Manaithiya, A.; Kumar, V.; Nazar, S.; Siddiqui, N. Recent Advancement in the Discovery and Development of Anti-Epileptic Biomolecules: An Insight into Structure Activity Relationship and Docking. *Eur. J. Pharm. Sci.* **2020**, *153*, No. 105494.

(7) Velez-Ruiz, N. J.; Meador, K. J. Neurodevelopmental Effects of Fetal Antiepileptic Drug Exposure. *Drug Saf* **2015**, *38* (3), 271.

(8) Ochoa-De La Paz, L. D.; Gulias-Cañizo, R.; Dábril Ruíz-Leyja, E.; Sánchez-Castillo, H.; Parodí, J.; Mexicana De Neurociencia, R.; Ochoa-De La Paz, L. The Role of GABA Neurotransmitter in the Human Central Nervous System, Physiology, and Pathophysiology. *Rev. Mex. Neuroci.* **2021**, *22* (2), 67−76.

(9) Sharma, R.; Nakamura, M.; Neupane, C.; Jeon, B. H.; Shin, H.; Melnick, S. M.; Glenn, K. J.; Jang, I. S.; Park, J. B. Positive Allosteric Modulation of GABAA Receptors by a Novel Antiepileptic Drug Cenobamate. *Eur. J. Pharmacol.* **2020**, *879*, No. 173117.

(10) Thapa, P.; Upadhyay, S. P.; Suo, W. Z.; Singh, V.; Gurung, P.; Lee, E. S.; Sharma, R.; Sharma, M. Chalcone and Its Analogs: Therapeutic and Diagnostic Applications in Alzheimer's Disease. *Bioorg Chem.* **2021**, *108*, No. 104681.

(11) Ventura-Salazar, I. A. Y.; Palacios-Can, F. J.; González-Maya, L.; Sánchez-Carranza, J. N.; Antunez-Mojica, M.; Razo-Hernández, R. S.; Alvarez, L. Finding a Novel Chalcone−Cinnamic Acid Chimeric Compound with Antiproliferative Activity against MCF-7 Cell Line Using a Free-Wilson Type Approach. *Molecules* **2023**, *28* (14), 5486.

(12) Królicka, E.; Kieć-Kononowicz, K.; Łażewska, D. Chalcones as Potential Ligands for the Treatment of Parkinson's Disease. *Pharmaceuticals* **2022**, *15* (7), 847.

(13) Christensen, S. B. Drugs That Changed Society: History and Current Status of the Early Antibiotics: Salvarsan, Sulfonamides, and β-Lactams. *Molecules* **2021**, *26* (19), 6057.

(14) Ueda, Y.; Doi, T.; Tokumaru, J.; Willmore, L. J. Effect of Zonisamide on Molecular Regulation of Glutamate and GABA Transporter Proteins during Epileptogenesis in Rats with Hippocampal Seizures. *Mol. Brain Res.* **2003**, *116* (1−2), 1−6.

(15) Siniatchkin, M.; Groppa, S.; Siebner, H.; Stephani, U. A Single Dose of Sulthiame Induces a Selective Increase in Resting Motor Threshold in Human Motor Cortex: A Transcranial Magnetic Stimulation Study. *Epilepsy Res.* **2006**, *72* (1), 18−24.

(16) Choo, B. K. M.; Kundap, U. P.; Johan Arief, M. F. bin; Kumari, Y.; Yap, J. L.; Wong, C. P.; Othman, I.; Shaikh, M. F. Effect of Newer Anti-Epileptic Drugs (AEDs) on the Cognitive Status in Pentylenetetrazol Induced Seizures in a Zebrafish Model. *Prog. Neuropsychopharmacol. Biol. Psychiatry* **2019**, *92*, 483−493.

(17) Ferreira, M. K. A.; da Silva, A. W.; dos Santos Moura, A. L.; Sales, K. V. B.; Marinho, E. M.; do Nascimento Martins Cardoso, J.; Marinho, M. M.; Bandeira, P. N.; Magalhães, F. E. A.; Marinho, E. S.; de Menezes, J. E. S. A.; dos Santos, H. S. Chalcones Reverse the Anxiety and Convulsive Behavior of Adult Zebrafish. *Epilepsy Behav.* **2021**, *117*, No. 107881.

(18) Novás, M.; Matos, M. J. The Role of Trifluoromethyl and Trifluoromethoxy Groups in Medicinal Chemistry: Implications for Drug Design. *Molecules* **2025**, *30* (14), 3009.
(19) Hanada, T. The Discovery and Development of Perampanel for the Treatment of Epilepsy. *Expert Opin Drug Discov* **2014**, *9* (4), 449−458.
(20) Mujawar, S.; Deshpande, A.; Bhambure, A.; Kolhe, S.; Prajapati, B. Computational Attitudes to Drug Discovery in Epilepsy. *Computational Neuropharmacology* **2025**, 313−334.
(21) Sommerfeld-Klatta, K.; Zielinska-Psuja, B.; Karazniewcz-Lada, M.; Glówka, F. K. New Methods Used in Pharmacokinetics and Therapeutic Monitoring of the First and Newer Generations of Antiepileptic Drugs (Aeds). *Molecules* **2020**, *25* (21), 5083.
(22) Ekins, S.; Lane, T. R. Applications of Artificial Intelligence in Drug Discovery for Neurological Diseases. *Neurotherapeutics* **2025**, *22*, No. e00624.
(23) Vatansever, S.; Schlessinger, A.; Wacker, D.; Kaniskan, H. Ü.; Jin, J.; Zhou, M. M.; Zhang, B. Artificial Intelligence and Machine Learning-aided Drug Discovery in Central Nervous System Diseases: State-of-the-arts and Future Directions. *Med. Res. Rev.* **2021**, *41* (3), 1427.
(24) Paul, D.; Sanap, G.; Shenoy, S.; Kalyane, D.; Kalia, K.; Tekade, R. K. Artificial Intelligence in Drug Discovery and Development. *Drug Discov Today* **2021**, *26* (1), 80.
(25) D'Amora, M.; Galgani, A.; Marchese, M.; Tantussi, F.; Faraguna, U.; De Angelis, F.; Giorgi, F. S. Zebrafish as an Innovative Tool for Epilepsy Modeling: State of the Art and Potential Future Directions. *Int. J. Mol. Sci.* **2023**, *24* (9), 7702.
(26) Hortopan, G. A.; Dinday, M. T.; Baraban, S. C. Zebrafish as a Model for Studying Genetic Aspects of Epilepsy. *Dis Model Mech* **2010**, *3* (3−4), 144−148.
(27) Hotz, J. M.; Thomas, J. R.; Katz, E. N.; Robey, R. W.; Horibata, S.; Gottesman, M. M. ATP-Binding Cassette Transporters at the Zebrafish Blood-Brain Barrier and the Potential Utility of the Zebrafish as an in Vivo Model. *Cancer Drug Resist.* **2021**, *4* (3), 620−633.
(28) Turrini, L.; Sorelli, M.; de Vito, G.; Credi, C.; Tiso, N.; Vanzi, F.; Pavone, F. S. Multimodal Characterization of Seizures in Zebrafish Larvae. *Biomedicines* **2022**, *10* (5), 951.
(29) Daina, A.; Michielin, O.; Zoete, V. SwissADME: A Free Web Tool to Evaluate Pharmacokinetics, Drug-Likeness and Medicinal Chemistry Friendliness of Small Molecules. *Sci. Rep* **2017**, *7* (1), 42717.
(30) Brenk, R.; Schipani, A.; James, D.; Krasowski, A.; Gilbert, I. H.; Frearson, J.; Wyatt, P. G. Lessons Learnt from Assembling Screening Libraries for Drug Discovery for Neglected Diseases. *ChemMedChem.* **2008**, *3* (3), 435−444.
(31) Heid, E.; Greenman, K. P.; Chung, Y.; Li, S. C.; Graff, D. E.; Vermeire, F. H.; Wu, H.; Green, W. H.; McGill, C. J. Chemprop: A Machine Learning Package for Chemical Property Prediction. *J. Chem. Inf Model* **2024**, *64* (1), 9−17.
(32) Fu, L.; Shi, S.; Yi, J.; Wang, N.; He, Y.; Wu, Z.; Peng, J.; Deng, Y.; Wang, W.; Wu, C.; Lyu, A.; Zeng, X.; Zhao, W.; Hou, T.; Cao, D. ADMETlab 3.0: An Updated Comprehensive Online ADMET Prediction Platform Enhanced with Broader Coverage, Improved Performance, API Functionality and Decision Support. *Nucleic Acids Res.* **2024**, *52* (W1), W422.
(33) Serrano-Regal, M. P.; Bayón-Cordero, L.; Ordaz, R. P.; Garay, E.; Limon, A.; Arellano, R. O.; Matute, C.; Sánchez-Gómez, M. V. Expression and Function of GABA Receptors in Myelinating Cells. *Front. Cell Neurosci.* **2020**, *14*, 256.
(34) Allen, M. J.; Sabir, S.; Sharma, S. GABA Receptor. *Trends Pharmacol. Sci.* **2023**, *2* (C), 62−64.
(35) Ghit, A.; Assal, D.; Al-Shami, A. S.; Hussein, D. E. E. GABAA Receptors: Structure, Function, Pharmacology, and Related Disorders. *J. Genet. Eng. Biotechnol.* **2021**, *19* (1), 123.
(36) Miller, P. S.; Aricescu, A. R. Crystal Structure of a Human GABAA Receptor. *Nature* **2014**, *512* (7514), 270−275.
(37) Imrie, F.; Bradley, A. R.; Deane, C. M. Generating Property-Matched Decoy Molecules Using Deep Learning. *Bioinformatics* **2021**, *37* (15), 2134−2141.
(38) Xie, H. B.; Sha, Y.; Wang, J.; Cheng, M. S. Some Insights into the Binding Mechanism of the GABAA Receptor: A Combined Docking and MM-GBSA Study. *J. Mol. Model* **2013**, *19* (12), 5489−5500.
(39) Neese, F. Software Update: The ORCA Program System—Version 5.0. *Wiley Interdiscip Rev. Comput. Mol. Sci.* **2022**, *12* (5), No. e1606.
(40) G09 | Gaussian.com. https://gaussian.com/glossary/g09/ (accessed May 3, 2025).
(41) Ahmad, V.; Khan, M. I.; Jamal, Q. M. S.; Alzahrani, F. A.; Albiheyri, R. Computational Molecular Docking and Simulation-Based Assessment of Anti-Inflammatory Properties of Nyctanthes Arbor-Tristis Linn Phytochemicals. *Pharmaceuticals* **2024**, *17* (1), 18.
(42) Badar, M. S.; Shamsi, S.; Ahmed, J.; Alam, Md. A. Molecular Dynamics Simulations: Concept. *Methods, and Applications* **2022**, *5*, 131−151.
(43) Dodda, L. S.; De Vaca, I. C.; Tirado-Rives, J.; Jorgensen, W. L. LigParGen Web Server: An Automatic OPLS-AA Parameter Generator for Organic Ligands. *Nucleic Acids Res.* **2017**, *45* (Web Server issue), W331−W336.
(44) Essmann, U.; Perera, L.; Berkowitz, M. L.; Darden, T.; Lee, H.; Pedersen, L. G. A Smooth Particle Mesh Ewald Method. *J. Chem. Phys.* **1995**, *103* (19), 8577−8593.
(45) Hess, B. P-LINCS: A Parallel Linear Constraint Solver for Molecular Simulation. *J. Chem. Theory Comput* **2008**, *4* (1), 116−122.
(46) Feas, D. A.; Igartúa, D. E.; Calienni, M. N.; Martinez, C. S.; Pifano, M.; Chiaramoni, N. S.; del Valle Alonso, S.; Prieto, M. J. Nutraceutical Emulsion Containing Valproic Acid (NE-VPA): A Drug Delivery System for Reversion of Seizures in Zebrafish Larvae Epilepsy Model. *J. Pharm. Investig* **2017**, *47* (5), 429−437.
(47) Baraban, S. C.; Taylor, M. R.; Castro, P. A.; Baier, H. Pentylenetetrazole Induced Changes in Zebrafish Behavior, Neural Activity and c-Fos Expression. *Neuroscience* **2005**, *131* (3), 759−768.
(48) Ursu, O.; Rayan, A.; Goldblum, A.; Oprea, T. I. Understanding Drug-Likeness. *Wiley Interdiscip Rev. Comput. Mol. Sci.* **2011**, *1* (5), 760−781.
(49) Bickerton, G. R.; Paolini, G. V.; Besnard, J.; Muresan, S.; Hopkins, A. L. Quantifying the Chemical Beauty of Drugs. *Nat. Chem.* **2012**, *4* (2), 90.
(50) Tijjani, H.; Olatunde, A.; Adegunloye, A. P.; Ishola, A. A. In Silico Insight into the Interaction of 4-Aminoquinolines with Selected SARS-CoV-2 Structural and Nonstructural Proteins. *Coronavirus Drug Discovery: Druggable Targets and In Silico Update: Volume 3* **2022**, 313−333.
(51) Morak-Młodawska, B.; Jeleń, M.; Martula, E.; Korlacki, R. Study of Lipophilicity and ADME Properties of 1,9-Diazaphenothiazines with Anticancer Action. *Int. J. Mol. Sci.* **2023**, *24* (8), 6970.
(52) Tsantili-Kakoulidou, A.; Demopoulos, V. J. Drug-like Properties and Fraction Lipophilicity Index as a Combined Metric. *ADMET DMPK* **2021**, *9* (3), 177.
(53) Veber, D. F.; Johnson, S. R.; Cheng, H. Y.; Smith, B. R.; Ward, K. W.; Kopple, K. D. Molecular Properties That Influence the Oral Bioavailability of Drug Candidates. *J. Med. Chem.* **2002**, *45* (12), 2615−2623.
(54) Doak, B. C.; Over, B.; Giordanetto, F.; Kihlberg, J. Oral Druggable Space beyond the Rule of 5: Insights from Drugs and Clinical Candidates. *Chem. Biol.* **2014**, *21* (9), 1115−1142.
(55) Spielvogel, C. P.; Schindler, N.; Schröder, C.; Stellnberger, S. L.; Wadsak, W.; Mitterhauser, M.; Papp, L.; Hacker, M.; Pichler, V.; Vraka, C. Enhancing Blood-Brain Barrier Penetration Prediction by Machine Learning-Based Integration of Novel and Existing, In Silico and Experimental Molecular Parameters from a Standardized Database. *J. Chem. Inf. Model.* **2025**, *65* (6), 2773−2784.
(56) Subramanian, G.; Kitchen, D. B. Computational Approaches for Modeling Human Intestinal Absorption and Permeability. *J. Mol. Model* **2006**, *12* (5), 577.

https://doi.org/10.1021/acsomega.5c04809
ACS Omega 2025, 10, 55325−55353

(57) Asano, D.; Takakusa, H.; Nakai, D. Oral Absorption of Middle-to-Large Molecules and Its Improvement, with a Focus on New Modality Drugs. *Pharmaceutics* **2024**, *16* (1), 47.
(58) Wu, D.; Chen, Q.; Chen, X.; Han, F.; Chen, Z.; Wang, Y. The Blood−Brain Barrier: Structure, Regulation, and Drug Delivery. *Signal Transduct. Target. Ther.* **2023**, *8* (1), 217.
(59) Delaney, J. S. ESOL: Estimating Aqueous Solubility Directly from Molecular Structure. *J. Chem. Inf. Comput. Sci.* **2004**, *44* (3), 1000−1005.
(60) Ran, Y.; Yalkowsky, S. H. Prediction of Drug Solubility by the General Solubility Equation (GSE). *J. Chem. Inf. Comput. Sci.* **2001**, *41* (2), 354−357.
(61) Crommelin, D. J. AAPS Advances in Pharmaceutical Sciences Series Series Editor.
(62) Bhalani, D. V.; Nutan, B.; Kumar, A.; Singh Chandel, A. K. Bioavailability Enhancement Techniques for Poorly Aqueous Soluble Drugs and Therapeutics. *Biomedicines* **2022**, *10* (9), 2055.
(63) Li, H.; Zhang, M.; Xiong, L.; Feng, W.; Williams, R. O. Bioavailability Improvement of Carbamazepine via Oral Administration of Modified-Release Amorphous Solid Dispersions in Rats. *Pharmaceutics* **2020**, *12* (11), 1023.
(64) Shayman, J. A.; Abe, A. DRUG INDUCED PHOSPHOLIPIDOSIS: AN ACQUIRED LYSOSOMAL STORAGE DISORDER. *Biochim. Biophys. Acta* **2013**, *1831* (3), 602.
(65) Wei, W.; Cherukupalli, S.; Jing, L.; Liu, X.; Zhan, P. Fsp3: A New Parameter for Drug-Likeness. *Drug Discovery Today* **2020**, *25*, 1839−1845.
(66) Wu, D.; Chen, Q.; Chen, X.; Han, F.; Chen, Z.; Wang, Y. The Blood−Brain Barrier: Structure, Regulation, and Drug Delivery. *Signal Transduction and Targeted Therapy 2023 8:1* **2023**, *8* (1), 1−27.
(67) Pardridge, W. M. Drug Transport across the Blood−Brain Barrier. *Journal of Cerebral Blood Flow & Metabolism* **2012**, *32* (11), 1959.
(68) Abbott, N. J. Blood−Brain Barrier Structure and Function and the Challenges for CNS Drug Delivery. *J. Inherit. Metab. Dis.* **2013**, *36* (3), 437−449.
(69) Susa, S. T.; Hussain, A.; Preuss, C. V. Drug Metabolism. *Pharmacognosy: Fundamentals, Applications, and Strategies*, 2nd ed.; Academic Press, 2023; pp 597−624.
(70) Sychev, D. A.; Ashraf, G. M.; Svistunov, A. A.; Maksimov, M. L.; Tarasov, V. V.; Chubarev, V. N.; Otdelenov, V. A.; Denisenko, N. P.; Barreto, G. E.; Aliev, G. The Cytochrome P450 Isoenzyme and Some New Opportunities for the Prediction of Negative Drug Interaction in Vivo. *Drug Des Devel Ther* **2018**, *12*, 1147−1156.
(71) Flaten, H. K.; Kim, H. S.; Campbell, J.; Hamilton, L.; Monte, A. A. CYP2C19 Drug-Drug and Drug-Gene Interactions in ED Patients. *Am. J. Emerg Med.* **2016**, *34* (2), 245.
(72) Patsalos, P. N.; Perucca, E. Clinically Important Drug Interactions in Epilepsy: General Features and Interactions between Antiepileptic Drugs. *Lancet Neurology* **2003**, *2* (6), 347−356.
(73) Galetin, A.; Zhang, L.; Rodrigues, A. D.; Huang, S. M.Drug-Drug Interactions. *Atkinson's Principles of Clinical Pharmacology*; Elsevier, 2022; pp 241−265.
(74) Liu, W.; He, M.; Li, Y.; Peng, Z.; Wang, G. A Review on Synthetic Chalcone Derivatives as Tubulin Polymerisation Inhibitors. *J. Enzyme Inhib Med. Chem.* **2022**, *37* (1), 9.
(75) Ménez, C.; Sutra, J. F.; Prichard, R.; Lespine, A. Relative Neurotoxicity of Ivermectin and Moxidectin in Mdr1ab (−/−) Mice and Effects on Mammalian GABA(A) Channel Activity. *PLoS Negl Trop Dis* **2012**, *6* (11), No. e1883.
(76) Yu, C.; Yuan, M.; Yang, H.; Zhuang, X.; Li, H. P-Glycoprotein on Blood-Brain Barrier Plays a Vital Role in Fentanyl Brain Exposure and Respiratory Toxicity in Rats. *Toxicol. Sci.* **2018**, *164* (1), 353−362.
(77) Mendell, J.; Zahir, H.; Matsushima, N.; Noveck, R.; Lee, F.; Chen, S.; Zhang, G.; Shi, M. Drug-Drug Interaction Studies of Cardiovascular Drugs Involving P-Glycoprotein, an Efflux Transporter, on the Pharmacokinetics of Edoxaban, an Oral Factor Xa Inhibitor. *American Journal of Cardiovascular Drugs* **2013**, *13* (5), 331.
(78) Kardoost, M.; Hajizadeh-Saffar, E.; Ghorbanian, M. T.; Ghezelayagh, Z.; Pooshang Bagheri, K.; Behdani, M.; Habibi-Anbouhi, M. Genotoxicity Assessment of Antiepileptic Drugs (AEDs) in Human Embryonic Stem Cells. *Epilepsy Res.* **2019**, *158*, No. 106232.
(79) Valproate. *LiverTox: Clinical and Research Information on Drug-Induced Liver Injury*, 2020.
(80) Hernandez-Diaz, S.; Huybrechts, K. F.; Desai, R. J.; Cohen, J. M.; Mogun, H.; Pennell, P. B.; Bateman, B. T.; Patorno, E. Topiramate Use Early in Pregnancy and the Risk of Oral Clefts: A Pregnancy Cohort Study. *Neurology* **2018**, *90* (4), No. e342.
(81) Kim, D.; Guengerich, F. P. CYTOCHROME P450 ACTIVATION OF ARYLAMINES AND HETEROCYCLIC AMINES. *Annu. Rev. Pharmacol. Toxicol.* **2025**, *45* (11), 27−49.
(82) Bhaiya, P.; Roychowdhury, S.; Vyas, P. M.; Doll, M. A.; Hein, D. W.; Svensson, C. K. BIOACTIVATION, PROTEIN HAPTENATION, AND TOXICITY OF SULFAMETHOXAZOLE AND DAPSONE IN NORMAL HUMAN DERMAL FIBROBLASTS. *Toxicol. Appl. Pharmacol.* **2006**, *215* (2), 158.
(83) You, C.; Wang, J.; Dai, X.; Wang, Y. Transcriptional Inhibition and Mutagenesis Induced by N-Nitroso Compound-Derived Carboxymethylated Thymidine Adducts in DNA. *Nucleic Acids Res.* **2015**, *43* (2), 1012−1018.
(84) Callan, H. E.; Jenkins, R. E.; Maggs, J. L.; Lavergne, S. N.; Clarke, S. E.; Naisbitt, D. J.; Kevin Park, B. Multiple Adduction Reactions of Nitroso Sulfamethoxazole with Cysteinyl Residues of Peptides and Proteins: Implications for Hapten Formation. *Chem. Res. Toxicol.* **2009**, *22* (5), 937−948.
(85) Möller, C.; Davis, W. C.; Thompson, V. R.; Marí, F.; Decaprio, A. P. Proteomic Analysis of Thiol Modifications and Assessment of Structural Changes in Hemoglobin Induced by the Aniline Metabolites N-Phenylhydroxylamine and Nitrosobenzene. *Sci. Rep* **2017**, *7* (1), 14794.
(86) Maldifassi, M. C.; Baur, R.; Pierce, D.; Nourmahnad, A.; Forman, S. A.; Sigel, E. Novel Positive Allosteric Modulators of GABAA Receptors with Anesthetic Activity. *Sci. Rep* **2016**, *6*, 25943.
(87) Vega Alanis, B. A.; Iorio, M. T.; Silva, L.; Bampali, K.; Ernst, M.; Schnürch, M.; Mihovilovic, M. D. Allosteric GABAA Receptor Modulators—A Review on the Most Recent Heterocyclic Chemotypes and Their Synthetic Accessibility. *Molecules* **2020**, *25* (4), 999.
(88) Klausberger, T.; Fuchs, K.; Mayer, B.; Ehya, N.; Sieghart, W. GABA(A) Receptor Assembly. Identification and Structure of Γ2 Sequences Forming the Intersubunit Contacts with A1 and B3 Subunits. *J. Biol. Chem.* **2000**, *275* (12), 8921−8928.
(89) Carugo, O.; Pongor, S. A Normalized Root-Mean-Spuare Distance for Comparing Protein Three-Dimensional Structures. *Protein Sci.* **2001**, *10* (7), 1470.
(90) Huang, N.; Shoichet, B. K.; Irwin, J. J. Benchmarking Sets for Molecular Docking. *J. Med. Chem.* **2006**, *49* (23), 6789.
(91) Bender, B. J.; Gahbauer, S.; Luttens, A.; Lyu, J.; Webb, C. M.; Stein, R. M.; Fink, E. A.; Balius, T. E.; Carlsson, J.; Irwin, J. J.; Shoichet, B. K. A Practical Guide to Large-Scale Docking. *Nat. Protoc* **2021**, *16* (10), 4799−4832.
(92) Wilcken, R.; Zimmermann, M. O.; Lange, A.; Joerger, A. C.; Boeckler, F. M. Principles and Applications of Halogen Bonding in Medicinal Chemistry and Chemical Biology. *J. Med. Chem.* **2013**, *56* (4), 1363−1388.
(93) Reynald, R. L.; Sansen, S.; Stout, C. D.; Johnson, E. F. Structural Characterization of Human Cytochrome P450 2C19: ACTIVE SITE DIFFERENCES BETWEEN P450s 2C8, 2C9, AND 2C19. *J. Biol. Chem.* **2012**, *287* (53), 44581−44591.
(94) Stoll, F.; Liesener, S.; Hohlfeld, T.; Schrör, K.; Fuchs, P. L.; Höltje, H. D. Pharmacophore Definition and Three-Dimensional Quantitative Structure-Activity Relationship Study on Structurally Diverse Prostacyclin Receptor Agonists. *Mol. Pharmacol.* **2002**, *62* (5), 1103−1111.
(95) Li, Q. Application of Fragment-Based Drug Discovery to Versatile Targets. *Front. Mol. Biosci.* **2020**, *7*, 180.

(96) Bapurao Dhande, M.; Krishna Chaitanya, G.; Tukaram Tayade, D.; Jadhao, S. Z.; Author, C. Global Reactivity Descriptors, Optimized Parameters and Hydration Free Energy of Sodium and Potassium Salt of Amino Acids. *Int. J. Res. Eng. Sci.* **2023**, *11* (9), 24−29.
(97) Bhatia, M. An Overview of Conceptual-DFT Based Insights into Global Chemical Reactivity of Volatile Sulfur Compounds (VSCs). *Computational Toxicology* **2024**, *29*, No. 100295.
(98) Boukabcha, N.; Direm, A.; Drissi, M.; Megrouss, Y.; Khelloul, N.; Dege, N.; Tuna, M.; Chouaih, A. Synthesis, Structural Determination, Hirshfeld Surface Analysis, 3D Energy Frameworks, Electronic and (Static, Dynamic) NLO Properties of o-Nitro-acetanilide (o-NAA): A Combined Experimental and Quantum Chemical Study. *Inorg. Chem. Commun.* **2021**, *133*, No. 108884.
(99) Yu, J.; Su, N. Q.; Yang, W. Describing Chemical Reactivity with Frontier Molecular Orbitalets. *JACS Au* **2022**, *2* (6), 1383−1394.
(100) Uzzaman, M.; Ahsan, A.; Uddin, M. N. Comparative Assessment of Some Benzodiazepine Drugs Based on Density Functional Theory, Molecular Docking, and ADMET Studies. *European Journal of Chemistry* **2021**, *12* (4), 412−418.
(101) Yang, C.; Li, X.; Zhou, N.; Chen, B.; Dong, H.; Jin, J.; Hu, X.; Huang, T.; Shen, L.; Yi, J.; Wang, Q.; Wang, J.; Ouyang, D. The Relationships between Direct Substituents, Aromaticity and Kinetic Stability of Pentazole Ring. *FirePhysChem.* **2023**, *3* (4), 350−355.
(102) Hadigheh Rezvan, V. Molecular Structure, HOMO−LUMO, and NLO Studies of Some Quinoxaline 1,4-Dioxide Derivatives: Computational (HF and DFT) Analysis. *Results Chem.* **2024**, *7*, No. 101437.
(103) Choudhary, V. K.; Bhatt, A. K.; Dash, D.; Sharma, N. DFT Calculations on Molecular Structures, HOMO−LUMO Study, Reactivity Descriptors and Spectral Analyses of Newly Synthesized Diorganotin(IV) 2-Chloridophenylacetohydroxamate Complexes. *J. Comput. Chem.* **2019**, *40* (27), 2354−2363.
(104) Govindarajan, M.; Karabacak, M.; Periandy, S.; Tanuja, D. Spectroscopic (FT-IR, FT-Raman, UV and NMR) Investigation and NLO, HOMO−LUMO, NBO Analysis of Organic 2,4,5-Trichloroaniline. *Spectrochim Acta A Mol. Biomol Spectrosc* **2012**, *97*, 231−245.
(105) Pearson, R. G. Chemical Hardness and Density Functional Theory. *J. Chem. Sci.* **2005**, *117* (5), 369−377.
(106) Mulliken, R. S. Electronic Population Analysis on LCAO−MO Molecular Wave Functions. *I. J. Chem. Phys.* **1955**, *23* (10), 1833−1840.
(107) Morales-Bayuelo, A.; Sánchez-Márquez, J.; Vivas-Reyes, R.; Kaya, S. Study Anti-Viral Drugs for Their Efficiency against Multiple SARS CoV-2 Drug Targets within Molecular Docking, Molecular Quantum Similarity, and Chemical Reactivity Indices Frameworks. *F1000Research 2024 13:270* **2024**, *13*, 270.
(108) Mohamed, A.; Visco, D. P.; Breimaier, K.; Bastidas, D. M. Effect of Molecular Structure on the B3LYP-Computed HOMO-LUMO Gap: A Structure − Property Relationship Using Atomic Signatures. *ACS Omega* **2025**, *10*, 2799−2808.
(109) Meng, X.-Y.; Zhang, H.-X.; Mezei, M.; Cui, M. Molecular Docking: A Powerful Approach for Structure-Based Drug Discovery. *Curr. Comput. Aided Drug Des* **2011**, *7* (2), 146.
(110) Hollingsworth, S. A.; Dror, R. O. Molecular Dynamics Simulation for All. *Neuron* **2018**, *99* (6), 1129−1143.
(111) Alturki, N. A.; Mashraqi, M. M.; Alzamami, A.; Alghamdi, Y. S.; Alharthi, A. A.; Asiri, S. A.; Ahmad, S.; Alshamrani, S. In-Silico Screening and Molecular Dynamics Simulation of Drug Bank Experimental Compounds against SARS-CoV-2. *Molecules* **2022**, *27* (14), 4391.
(112) Sargsyan, K.; Grauffel, C.; Lim, C. How Molecular Size Impacts RMSD Applications in Molecular Dynamics Simulations. *J. Chem. Theory Comput* **2017**, *13* (4), 1518−1524.
(113) Peulen, T. O.; Hengstenberg, C. S.; Biehl, R.; Dimura, M.; Lorenz, C.; Valeri, A.; Folz, J.; Hanke, C. A.; Ince, S.; Vöpel, T.; Faragó, B.; Gohlke, H.; Klare, J. P.; Stadler, A. M.; Seidel, C. A. M.; Herrmann, C. Integrative Dynamic Structural Biology Unveils Conformers Essential for the Oligomerization of a Large GTPase. *Elife* **2023**, *12*, No. e79565.
(114) Lobanov, M. Y.; Bogatyreva, N. S.; Galzitskaya, O. V. Radius of Gyration as an Indicator of Protein Structure Compactness. *Mol. Biol.* **2008**, *42* (4), 623−628.
(115) Bagewadi, Z. K.; Yunus Khan, T. M.; Gangadharappa, B.; Kamalapurkar, A.; Mohamed Shamsudeen, S.; Yaraguppi, D. A. Molecular Dynamics and Simulation Analysis against Superoxide Dismutase (SOD) Target of Micrococcus Luteus with Secondary Metabolites from Bacillus Licheniformis Recognized by Genome Mining Approach. *Saudi J. Biol. Sci.* **2023**, *30* (9), No. 103753.
(116) Spreitzer, E.; Usluer, S.; Madl, T. Probing Surfaces in Dynamic Protein Interactions. *J. Mol. Biol.* **2020**, *432* (9), 2949−2972.
(117) Du, X.; Li, Y.; Xia, Y. L.; Ai, S. M.; Liang, J.; Sang, P.; Ji, X. L.; Liu, S. Q. Insights into Protein−Ligand Interactions: Mechanisms, Models, and Methods. *Int. J. Mol. Sci.* **2016**, *17* (2), 144.
(118) Zhao, Q.; Holmes, G. L. Repetitive Seizures in the Immature Brain. *Models of Seizures and Epilepsy* **2006**, 341−350.
(119) Cho, S. J.; Byun, D.; Nam, T. S.; Choi, S. Y.; Lee, B. G.; Kim, M. K.; Kim, S. Zebrafish as an Animal Model in Epilepsy Studies with Multichannel EEG Recordings. *Scientific Reports 2017 7:1* **2017**, *7* (1), 1−10.
(120) Kundap, U. P.; Kumari, Y.; Othman, I.; Shaikh, M. F. Zebrafish as a Model for Epilepsy-Induced Cognitive Dysfunction: A Pharmacological, Biochemical and Behavioral Approach. *Front Pharmacol* **2017**, *8* (AUG), 515.
(121) Gawel, K.; Langlois, M.; Martins, T.; van der Ent, W.; Tiraboschi, E.; Jacmin, M.; Crawford, A. D.; Esguerra, C. V. Seizing the Moment: Zebrafish Epilepsy Models. *Neurosci Biobehav Rev.* **2020**, *116*, 1−20.
(122) Bertoncello, K. T.; Bonan, C. D. Zebrafish as a Tool for the Discovery of Anticonvulsant Compounds from Botanical Constituents. *Eur. J. Pharmacol.* **2021**, *908*, No. 174342.
(123) Knap, B.; Nieoczym, D.; Kundap, U.; Kusio-Targonska, K.; Kukula-Koch, W.; Turski, W. A.; Gawel, K. Zebrafish as a Robust Preclinical Platform for Screening Plant-Derived Drugs with Anticonvulsant Properties—a Review. *Front. Mol. Neurosci.* **2023**, *16*, 1221665.
(124) Mussulini, B. H. M.; Leite, C. E.; Zenki, K. C.; Moro, L.; Baggio, S.; Rico, E. P.; Rosemberg, D. B.; Dias, R. D.; Souza, T. M.; Calcagnotto, M. E.; Campos, M. M.; Battastini, A. M.; de Oliveira, D. L. Seizures Induced by Pentylenetetrazole in the Adult Zebrafish: A Detailed Behavioral Characterization. *PLoS One* **2013**, *8* (1), No. e54515.
(125) Shaw, P. A. G.; Panda, S. K.; Stanca, A.; Luyten, W. Optimization of a Locomotion-Based Zebrafish Seizure Model. *J. Neurosci Methods* **2022**, *375*, No. 109594.